

# Localized gravity/topography admittance and correlation spectra on Mars: Implications for regional and global evolution

Patrick J. McGovern<sup>1</sup>, Sean C. Solomon<sup>2</sup>, David E. Smith<sup>3,4</sup>, Maria T. Zuber<sup>4</sup>, Mark Simons<sup>5</sup>, Mark A. Wieczorek<sup>4</sup>, Roger J. Phillips<sup>6</sup>, Gregory A. Neumann<sup>4</sup>, Oded Aharonson<sup>4</sup>, and James W. Head<sup>7</sup>

**Abstract.** From gravity and topography data collected by the Mars Global Surveyor spacecraft we calculate gravity/topography admittances and correlations in the spectral domain and compare them to those predicted from models of lithospheric flexure. On the basis of these comparisons we estimate the thickness of the Martian elastic lithosphere ( $T_e$ ) required to support the observed topographic load since the time of loading. We convert  $T_e$  to estimates of heat flux and thermal gradient in the lithosphere through a consideration of the response of an elastic/plastic shell. In regions of high topography on Mars (e.g., the Tharsis rise and associated shield volcanoes), the mass-sheet (small-amplitude) approximation for the calculation of gravity from topography is inadequate. A correction that accounts for finite-amplitude topography tends to increase the amplitude of the predicted gravity signal at spacecraft altitudes. Proper implementation of this correction requires the use of radii from the center of mass (collectively known as the planetary “shape”) in lieu of “topography” referenced to a gravitational equipotential. Anomalously dense surface layers or buried excess masses are not required to explain the observed admittances for the Tharsis Montes or Olympus Mons volcanoes when this correction is applied. Derived  $T_e$  values generally decrease with increasing age of the lithospheric load, in a manner consistent with a rapid decline of mantle heat flux during the Noachian and more modest rates of decline during subsequent epochs.

## 1. Introduction

Variations in the heat flow from the interior to the surface of a planet can have pronounced effects on tectonic, magmatic, and geological processes. In the absence of direct measurements, surface heat flow can be estimated from the elastic or mechanical thickness of the lithosphere, because the base of the lithosphere is defined approximately by a temperature at which crustal or mantle rocks undergo ductile flow on a geological time scale. Estimates of elastic lithosphere thickness ( $T_e$ ) and loading styles for Mars have been derived from gravity, topography, and image data sets.

In this paper, we present new estimates for  $T_e$  and heat flow on Mars from relationships between gravity and topography, making use of new measurements of both fields by the Mars Global Surveyor (MGS) mission.

Many earlier studies exploited the distribution of tectonic features associated with large lithospheric loads to constrain lithospheric structure at the time of loading by means of comparisons with predictions of fault types and orientations derived from flexural models. In such analyses, topographic information is used to estimate the (surface) load and is usually the primary input to the models. For example, *Comer et al.* [1985] compared modeled surface stresses with the radial range of graben concentric to large volcanic loads, yielding best-fit  $T_e$  values in the range 20 to 50 km for the volcanoes of Tharsis Montes, Alba Patera, and Elysium Mons and  $T_e > 120$  km for the Isidis basin mascon. *Hall et al.* [1986] confirmed the *Comer et al.* [1985] estimate of  $T_e$  (50 km) at Elysium Mons. The absence of prominent concentric graben around the Olympus Mons volcano led *Thurber and Toksöz* [1978] to derive a lower bound on  $T_e$  ( $> 150$  km). *Janle and Jannsen* [1986] combined this tectonic constraint at Olympus Mons with an analysis of gravity and topography to derive the limits  $140 \text{ km} \leq T_e \leq 230 \text{ km}$ . *Schultz and Lin* [2001] estimated the lithospheric thermal gradient at Valles Marineris from boundary element models of rift flank uplift and obtained values consistent with  $T_e > 60$  km. *Watters and Schultz* [2001] modeled the formation of thrust fault topography at Amenthes Rupes, determining the maximum depth of faulting to be 25–30 km.

Other studies of lithospheric characteristics on Mars have relied primarily on relationships between gravity and topography, compared either directly as a function of position or

<sup>1</sup>Lunar and Planetary Institute, Houston, Texas

<sup>2</sup>Department of Terrestrial Magnetism, Carnegie Institution of Washington, Washington, D.C.

<sup>3</sup>NASA Goddard Flight Center, Greenbelt, Maryland

<sup>4</sup>Department of Earth, Atmospheric, and Planetary Sciences, Massachusetts Institute of Technology, Cambridge, Massachusetts

<sup>5</sup>Division of Geological and Planetary Sciences, California Institute of Technology, Pasadena, California

<sup>6</sup>Department of Earth and Planetary Sciences, Washington University, St. Louis, Missouri

<sup>7</sup>Department of Geological Sciences, Brown University, Providence, Rhode Island

in the harmonic domain. For example, *Turcotte et al.* [1981] used thin spherical-shell flexure models to demonstrate that long-wavelength topography on Mars is primarily supported by membrane stresses in the lithosphere. Under the thin-shell approximation, the ratio of spherical harmonic coefficients of gravitational potential to topography (for harmonic degrees 4 to 7) yielded a (global)  $T_e$  estimate of 175 km. *Banerdt et al.* [1982, 1992] and *Sleep and Phillips* [1985] combined gravity information with tectonic constraints to infer aspects of subsurface compensation and loading for assumed values of  $T_e$  on regional (Tharsis) to global scales. *Janle and Erkul* [1991] modeled gravity and topography data to evaluate end-member compensation models for and possible mantle density anomalies beneath the Tharsis Montes and Alba Patera. *Anderson and Grimm* [1998] analyzed harmonic expansions for gravity and topography in the vicinity of Valles Marineris, inferring  $T_e < 30$  km and heat flux consistent with a wide-rift origin [*Buck*, 1991] and regularly-spaced chasms.

Several studies have taken advantage of the new MGS gravity and topography data. From an analysis of early MGS gravity and topography, *Anderson and Banerdt* [2000] interpreted a sharp dropoff in gravity/topography admittance at wavelengths shorter than 1000 km as evidence for a deep mantle load compensating the Valles Marineris troughs. *Arkani-Hamed* [2000], also from early MGS data, estimated  $T_e$  (80–100 km) for Olympus Mons and the Tharsis Montes and concluded that anomalously dense subsurface loads are present beneath these structures. *Turcotte et al.* [2002] used point correlations of gravity and topography to obtain values for mean crustal thickness (90 km) and density (2960 kg/m<sup>3</sup>). From one-dimensional wavelet transforms they inferred a globally-averaged elastic lithosphere thickness of 90 km. *McKenzie et al.* [2002] used cartesian-domain admittance techniques to estimate  $T_e$  at Tharsis (70 km), Elysium (27 km), and the southern hemisphere (14.5 km). They inferred that crustal densities at Tharsis (3.0 kg/m<sup>3</sup>) are similar to measured densities of Martian meteorites but that the crustal density at Valles Marineris is substantially lower (2.35 kg/m<sup>3</sup>), suggestive of a large fraction of ice within the crust.

In this paper, we exploit several recent advances in the harmonic analysis of gravity and topography. First, we localize the gravity and topography spectra with the spatio-spectral windowing method of *Simons et al.* [1997]. This formalism allows the inference of lithospheric properties for specific features rather than global averages (as, for example, by *Turcotte et al.* [1981]). Further, the large dynamic range of Martian topography renders inaccurate the first-order mass-sheet approximation for calculating gravity from relief of density interfaces, an essential step in modeling. We account for the effects of finite-amplitude relief with the higher-order gravity calculation of *Wieczorek and Phillips* [1998]. With the new gravity and topographic relief data from MGS as well as improved models, we explore the implications of localized admittances for the compensation of surface features and the thermal evolution of the planet.

First, we compare observed admittance and correlation spectra with those predicted by spherical shell flexure models, in order to estimate the effective elastic lithosphere thickness  $T_e$  at the time of loading. The resulting  $T_e$  estimates can be used to constrain the thermal history of the lithosphere. We apply a standard procedure based on the properties of elastic/plastic flexed plates [*McNutt*, 1984] to convert  $T_e$  into estimates of thermal gradient and heat flux in the lithosphere. We compare these results with those obtained from earlier estimates of  $T_e$  for Mars [e.g., *Solomon and Head*, 1990], and we then evaluate the implications of our estimates for the thermal evolution of the planet.

## 2. Method

Following *Smith et al.* [1999a], we define topography  $H$  as a function of colatitude  $\theta$  and longitude  $\phi$  as

$$H(\theta, \phi) = S(\theta, \phi) - A(\theta, \phi), \quad (1)$$

where  $S$  is radius from the center of mass and  $A$  is the height of the reference equipotential surface, or areoid. We refer to the field  $S(\theta, \phi)$  as the planetary shape. This definition of “topography” is always followed in this paper but differs from some past usage. For example, *Wieczorek and Phillips* [1998] consider “topography  $H(\theta, \phi)$  referenced to a radius  $D$ ,” their  $H$  is thus equivalent to  $S$  to within the addition of a constant. “Topography” is often used as a generic term for height or relief. The distinction between topography (as defined by equation 1) and radius is not generally significant for bodies with modest rotational flattening and small excursions of the reference gravitational potential from a spheroid, such as Venus. However, areoid heights can exceed 1 km in the Tharsis region of Mars [*Smith et al.*, 1999b], and distinguishing between topography and shape is important for quantitative modeling, as we demonstrate below.

We calculate gravity/shape admittances and correlations as functions of spherical harmonic degree using the spatio-spectral localization approach of *Simons et al.* [1997]. We localize within axisymmetric windows of fixed widths specified by harmonic degree  $L_{win} = 5, 10, \text{ or } 15$  (corresponding to dimensions of 4000, 2000, or 1400 km, respectively). We generate gravity models under the assumption that the observed topography consists of material of density  $\rho_l$  acting as a surface load on a thin, spherical elastic shell [*Turcotte et al.*, 1981]. We also allow for sublithospheric or bottom loading, correlated with topography and parameterized by the ratio  $f$  of the magnitude of the bottom load to that of the top load [*Forsyth*, 1985]. Details of this methodology are given in Appendices A and B.

The elastic lithosphere thickness  $T_e$  of the shell is varied to generate a suite of models. We calculate localized admittances versus spherical harmonic degree  $l$  for observed shape and gravity and for shape and gravity predicted from the flexure models. By comparing observed and modeled admittances, we estimate  $T_e$  at time of loading, under the assumptions that all relief within the localization window is compensated by a single mechanism and that the lithospheric response is subsequently “frozen in.” In regions that have undergone reheating or stress relaxation after loading (violating the assumption that flexural stresses are frozen-in), lithospheric thickness estimates will be lower bounds on  $T_e$  at the time of loading [*Albert and Phillips*, 2000]. A successful estimate of  $T_e$  requires an admittance fit over a significant wavenumber band as well as a strong correlation (generally near 1) between gravity and shape over the same band. Our estimates of  $T_e$  are most accurate for regions exhibiting small admittance fluctuations, small formal errors, and high correlations. Estimates of  $T_e$  cannot be obtained in this manner for regions with strongly-varying

or negative admittances and negative or near-zero correlations, including the topographically smooth northern lowlands of Mars and the largest impact basins. Models for such regions require additional assumptions about buried loads. In particular, shape/gravity correlations with magnitudes near zero indicate the failure of simple models such as those presented here, suggesting the presence of multiple loading mechanisms [e.g., *Forsyth, 1985*]. For such areas, we do not interpret admittance spectra in terms of  $T_e$ , although we do comment on potential contributing modes of loading.

To evaluate the sensitivity of the solution fit to variations in the model parameters, including  $T_e$ , the reference crustal thickness  $T_{cr}$ , the load density  $\rho_l$ , and the bottom loading fraction  $f$ , we carry out trade-off analyses among these parameters. We calculate the root-mean-square (r.m.s.) misfit between the observed admittance spectrum and the predicted admittance for each suite of model parameters. We then display contours of r.m.s. misfit on a two-parameter projection of the chosen parameter space, to identify regions with favorable solutions. We reject models having r.m.s. misfit greater than 10 mGal/km, a value that in general exceeds the largest formal errors on admittance. We prefer models with r.m.s. misfits less than 5 mGal/km, although not all regions or parameter ranges satisfy such a criterion.

## 2.1. Data

The MGS mission has yielded representations of Martian gravity and topography substantially superior in resolution and accuracy to earlier solutions. The Mars Orbiter Laser Altimeter (MOLA) has obtained more than 671 million measurements of Martian topography [*Smith et al., 2001*] accurate to 1 m, with a range resolution of 37.5 cm, from which a spherical harmonic expansion of topography to degree and order 1152 has been determined [*Smith et al., 2001*]. The MGS Radio Science experiment obtained Doppler tracking residuals from which spherical harmonic representations of the gravitational potential of Mars have been derived [*Smith et al., 1999b*]. In this paper, we use potential field expansion mgm1025 [*Lemoine et al., 2001*]. We truncate this expansion at harmonic degree and order 60, beyond which errors can exceed 100%. The topography and shape of Mars for harmonic degrees 1 to 60 are shown in Figures 1a and 1b. The gravity field for degrees 2 to 60 is shown in Figure 1c, with the  $J_2$  term reduced by 95% to account for the hydrostatic flattening contribution [*Folkner et al., 1997*].

## 2.2. Admittance Localization

We employ the spatio-spectral localization technique of *Simons et al. [1997]* to obtain gravity/shape admittance ( $F_l$ ) and correlation ( $r_l$ ) spectra as functions of position on Mars. Following *Simons et al. [1997]*, we consider the shape

**Figure 1.** Spherical harmonic expansions of MGS data for Mars, shown in the Winkel Tripel projection using the Generic Mapping Tools (GMT) software [*Wessel and Smith, 1991*]. (a) Topography relative to the areoid defined by gravity model mgm1004d [*Lemoine et al., 2001*], for degrees 1 to 60. (b) Shape (radius from the center of mass) relative to a radius datum of 3389.5 km. (c) Spherical harmonic expansion (degrees 2 to 60) of the Martian gravity field [*Lemoine et al., 2001*]. The  $J_2$  term has been reduced by 95% to account for the hydrostatic flattening contribution [*Folkner et al., 1997*].

field  $S(\Omega)$  defined on the spherical domain  $\Omega = (\theta, \phi)$

$$S(\Omega) = \sum_{lm} s_{lm} Y_{lm}(\Omega), \quad (2)$$

where  $s_{lm}$  are the harmonic coefficients of degree  $l$  and order  $m$ , and  $Y_{lm}$  are the fully normalized spherical harmonics following the notation convention of *Edmonds [1957]*. Given a window function  $W(\Omega)$

$$W(\Omega) = \sum_{lm} w_{lm} Y_{lm}(\Omega), \quad (3)$$

we construct the localized version of  $S$  from

$$\Psi(\Omega) = W(\Omega)S(\Omega) = \sum_{lm} \psi_{lm} Y_{lm}(\Omega). \quad (4)$$

We then obtain the coefficients  $\psi_{lm}$  by

$$\psi_{lm} = \int S(\Omega)W(\Omega)Y_{lm}^*(\Omega)d\Omega, \quad (5)$$

where the asterisk denotes complex conjugation. This integral for this product of three spherical harmonics is evaluated with the Wigner 3-j symbols described in *Varshalovich et al. [1988]*. A similar set of localized coefficients,  $\gamma_{lm}$ , can be defined for  $\Gamma(\Omega)$ , the localized version of the gravity perturbation  $\Delta g$  (defined below).

The cross covariance of the  $S$  and  $\Delta g$  fields is [*Simons et al., 1997*]

$$\sigma_{\Psi\Gamma}^2(l) = \sum_m \psi_{lm}\gamma_{lm}^*. \quad (6)$$

The gravity/shape admittance spectrum is then given by

$$F_l = \frac{\sigma_{\Psi\Gamma}^2}{\sigma_{\Psi\Psi}^2}, \quad (7)$$

and the correlation spectrum is

$$r_l = \frac{\sigma_{\Psi\Gamma}^2}{\sqrt{\sigma_{\Psi\Psi}^2\sigma_{\Gamma\Gamma}^2}}, \quad (8)$$

where  $\sigma$  represents either auto- or cross-covariances of the localized fields [*Simons et al., 1997*].

In this paper, we localize harmonic fields with axisymmetric windows of constant diameter, described by  $L_{win}$  zonal harmonic coefficients. This choice restricts the permissible range of  $l$  in the windowed fields at both the low- ( $l \geq L_{win}$ ) and high-wavenumber ends ( $l \leq L_{obs} - L_{win}$ , where  $L_{obs}$  is the maximum degree of observation). In contrast to the scalable windows (for which  $L_{win}$  depends on  $l$ ) used in *Simons et al. [1997]*, a fixed window insures that the same geographical region or feature is analyzed through-

**Figure 2.** Harmonic expansions of localized shape  $S(\theta, \phi)$ , plotted in an orthographic projection, for windows with  $L_{win} = 5$  (upper right), 10 (lower left), and 15 (lower right). Full expansion (degrees 1–60) of  $S(\theta, \phi)$  is shown in upper left. Localized fields are expanded from degrees 5–55 for  $L_{win} = 5$ , 10–50 for  $L_{win} = 10$ , and 15–45 for  $L_{win} = 15$ . Windows are centered on Olympus Mons (19°N, 226.5°E).

out the permissible wavenumber band, an appealing property when studying a specific geologic province or construct. With a fixed window, we give up some spatial resolution at the shortest wavelengths in order to focus the analysis on a single region at all wavelengths allowed by the window. Due to this averaging of short wavelengths, the fixed window approach yields better noise bias characteristics at high  $l$  than scalable windows.

For this study, we choose windows with  $L_{win} = 5, 10,$  and  $15$  (equivalent to spatial scales of 4000, 2000, or 1400 km, respectively). Harmonic expansions of  $S(\theta, \phi)$ , localized with such windows, are shown in Figure 2. At Olympus Mons, localization with  $L_{win} = 5$  includes a substantial portion of the Tharsis rise (Figure 2, upper right). Increasing  $L_{win}$  narrows the window; for  $L_{win} = 10$  and  $15$ , only the topography of the Olympus Mons edifice is evident (Figure 2, lower left and right, respectively). For each feature, we interpret spectra obtained with the widest window (lowest  $L_{win}$ ) that isolates the topography of the feature in question, because increasing  $L_{win}$  decreases the available spectral resolution [Simons *et al.*, 1997]. Narrower features tend to require higher  $L_{win}$  values to isolate them from their surroundings.

### 2.3. Models

**2.3.1. Flexure solution.** We adopt a modified version of the formulation of *Turcotte et al.* [1981] for loading of a thin, elastic, homogeneous spherical shell; the effects of anisotropic lithospheric response (e.g., faulting) are not modeled. We acknowledge that spherical-shell flexure solutions have been subject to further development, to relax approximations regarding vertical normal stresses within the shell [e.g., “thick plate” solutions: *Banerdt et al.*, 1982; *Zhong and Zuber*, 2000] and horizontal stresses induced by topography [*Banerdt et al.*, 1982; *Banerdt*, 1986]. However, solutions for deflections generally differ by less than 10% [*Zhong and Zuber*, 2000] from those of thin-plate solutions [e.g., *Turcotte et al.*, 1981]. Inasmuch as modeled admittances depend only on deflections, not stresses, the solution adopted here is sufficient.

The solution of *Turcotte et al.* [1981] was modified to account for a load density  $\rho_l$  that differs from the crustal density  $\rho_c$  (see Appendix A). For models or suites of models where  $\rho_l$  and  $\rho_c$  are set to the same value (which may vary within a suite), we use the term surface density ( $\rho_s$ ) to identify the chosen value(s). Harmonic coefficients of deflection  $w_{ilm}$  are related to those of surface relief  $h_{ilm}$  by equations of the form

$$w_{ilm} = h_{ilm}\alpha_l, \quad (9)$$

where  $\alpha_l$  is a transfer function that depends on the type(s) of loading present (see Appendix A). Nominal values for model

**Table 1.** Nominal Parameter Values

Parameter Name	Symbol	Value	Units
Load density	$\rho_l$	2900	kg/m <sup>3</sup>
Crustal density	$\rho_c$	2900	kg/m <sup>3</sup>
Mantle density	$\rho_m$	3500	kg/m <sup>3</sup>
Bottom load density contrast	$\rho_b$	600	kg/m <sup>3</sup>
Reference crustal thickness	$T_{cr}$	50	km
Young’s modulus of lithosphere	$E$	$1 \times 10^{11}$	Pa
Poisson’s ratio of lithosphere	$\nu$	0.25	–

parameters are listed in Table 1. We assume that any flexural depression has been filled with material of density  $\rho_l$ . The manner by which loads, surface relief, and deflections are determined from topography is described in Appendix B. Loads are calculated using equipotentially-referenced topography rather than sphere-referenced radius. The resulting deflections are then summed with a reference equipotential  $A_{ref}$  corresponding to the hydrostatic component of  $J_2$  (see Table 2). These choices prevent the rotational flattening from being treated as a lithospheric load, under the presumption that the lithospheric response to flattening is locally isostatic.

**2.3.2. Potential from a density interface.** As *Wieczorek and Phillips* [1998] have demonstrated, the accurate calculation of potential anomalies arising from large-amplitude relief requires expansion of topography or shape to powers beyond first order. To this end, following *Wieczorek and Phillips* [1998], we expand the  $n$ th power of radius  $S$  (referenced to the mean radius  $R$ ):

$$S^n(\theta', \phi') = \sum_{i'l'm'} n_{s'l'm'} Y_{i'l'm'}(\theta', \phi'), \quad (10)$$

where  $Y_{i'l'm'}(\theta', \phi')$  is the fully normalized spherical harmonic of degree  $l$  and order  $m$  and  $i$  ranges from 1 to 2 for the  $\cos(m\phi)$  and  $\sin(m\phi)$  terms, respectively. The expression for the potential from the surface represented by  $S$ , at distance  $r$  from the center of the mass, is

$$U(r, \theta, \phi) = \frac{GM}{r} \sum_{ilm} \left(\frac{R}{r}\right)^l C_{ilm}^+ Y_{ilm}(\theta, \phi), \quad (11)$$

where

$$C_{ilm}^+ = \frac{4\pi\Delta\rho R^3}{M(2l+1)} \sum_{n=1}^{l+3} \frac{n_{silm}}{R^n n!} \frac{\prod_{j=1}^n (l+4-j)}{l+3}, \quad (12)$$

$M$  is the mass of Mars, and  $\Delta\rho$  is the density contrast (here equal to load density  $\rho_l$ ). Additional discussion of the rationale for this procedure is given in Appendix C.

**2.3.3. Model gravity calculation.** To calculate model gravity coefficients, we need to account for five density-contrast interfaces: the surface, the surface of the deflected crust, the deflected crust-mantle boundary, and the upper and lower surfaces of the bottom load. The density contrasts and reference depths associated with these interfaces are summarized in Table 2. The potential coefficients  $C_{ilm}^{total}$  are the sums of the coefficients, calculated by Equation 12, for the five interfaces, each upward continued from the appropriate reference level (Table 2):

$$C_{ilm}^{total} = C_{ilm}^s + C_{ilm}^c + \left(\frac{R - T_{cr}}{R}\right)^l C_{ilm}^{cm} + \left(\frac{R - z_b}{R}\right)^l [C_{ilm}^{bu} + C_{ilm}^{bl}], \quad (13)$$

**Figure 3.** Global gravity/shape admittance (left column) and correlation (right column) maps, in Winkel Tripel projections, localized at harmonic degrees 20, 35, and 50 (bottom to top), using a window of spectral width  $L_{win} = 10$ . Contours of topography (2-km interval) are superposed on the maps.

**Table 2.** Gravity Calculation

Interface	Interface Terms	Density Contrast	Reference Depth
Surface	$S$	$\rho_l$	0
Crustal surface	$h_b + w_t + A_{ref}$	$\rho_c - \rho_l$	0
Crust-mantle boundary	$h_b + w_t + A_{ref}$	$\rho_m - \rho_c$	$T_{cr}$
Bottom load	$w_b + h_b + w_t + A_{ref}$	$\rho_b$	$z_b$
Bottom load reference	$h_b + w_t + A_{ref}$	$-\rho_b$	$z_b$

Note that a reference areoid height  $A_{ref} = 0.95 \times J_2$  has been added to the height of all interfaces derived from the topographic (areoid-referenced) load prior to the gravity calculation, in order to avoid including the hydrostatic flattening of Mars in the lithospheric load. See Appendix B for the descriptions of surface and subsurface loading terms  $h_t, w_t, h_b$ , and  $w_b$ .

where  $s, c, cm, bu$ , and  $bl$  correspond to surface, deflected crustal surface, crust-mantle boundary, and upper and lower surfaces of the bottom load, respectively,  $T_{cr}$  is the reference crustal thickness, and  $z_b$  is the reference depth of the bottom load. The gravity perturbation  $\Delta g$  is given by

$$\Delta g = \frac{GM}{r^2} \sum_{ilm} \left(\frac{R}{r}\right)^l (l+1) C_{ilm}^{total} Y_{ilm}. \quad (14)$$

The effective model gravity coefficients  $G_{ilm}^{total} = (l+1) C_{ilm}^{total}$  are then localized by the scheme described above, enabling the generation of gravity/shape admittance and correlation spectra with which the observed spectra may be compared.

### 3. Results

#### 3.1. Admittance and Correlation: A Global View

Global maps of the gravity/shape admittance and correlation can be obtained by moving the spatio-spectral windows described above over the full spherical harmonic fields. One such map, localized at spectral degree 20 with  $L_{win} = 10$  (window diameter = 2400 km) is shown in Figure 3 (lower left). Several features stand out as relatively high-admittance regions, including Olympus Mons, Tharsis Montes, and Valles Marineris. Other high-admittance regions include a zone centered in the southern Utopia basin (part of which overlaps the Elysium rise) and an arcuate area cutting through Amazonis and Arcadia Planitiae. Low to moderate admittance values (generally less than 50 mGal/km) are typical in the southern hemisphere.

A map of gravity/shape correlation at degree 20 for  $L_{win} = 10$  (Figure 3, lower right) shows that the southern hemisphere of Mars is generally characterized by high gravity/shape correlation. The volcanic constructs Olympus Mons, Tharsis Montes, and Elysium rise have particularly high correlations, as does Valles Marineris. A significant fraction of the northern hemisphere has near-zero or negative correlations, as does the Isidis impact basin and a portion of the northeastern rim of the Hellas basin, suggested to be the site of a buried impact basin [Schultz and Frey, 1990]. Portions of the boundary between topographic and crustal thickness provinces [Zuber et al., 2000] to the south of Elysium and northwest of Isidis are characterized by a transition from high positive correlation in the southern uplands to near- or below-zero correlation in the lowlands. However, other regions near the so-called crustal dichotomy boundary, such as central Arabia Terra and Tempe Terra, exhibit low positive or near-zero correlations, respectively. Highly negative correlations are seen in part of the Utopia basin and centered on the Argyre basin, sites of gravity highs and topographic lows.

Admittances and correlations localized at degree 35 show important differences from those at degree 20. The Isidis and Argyre basins display positive rather than negative admittance and correlation (contrast lower left and right with

middle left and right in Figure 3). For  $l = 35$ , the Elysium rise is at the center of a high-admittance region rather than at the periphery, and the northern hemisphere exhibits more regions of positive admittance than for  $l = 20$ . In the northern hemisphere, many regions of extremely negative admittance at  $l = 20$  show extremely positive admittance at  $l = 35$ . For  $l = 35$  the high-admittance region surrounding central Tharsis and Valles Marineris covers much of Sinai, Solis, and Lunae Plana. Correlations along the eastern crustal dichotomy boundary at  $l = 35$  are similar to those for  $l = 20$ , except that those in Arabia Terra are near zero, while those for Tempe Terra are large and exceed  $> 0.5$ . Several patches of low positive correlation ( $< 0.5$ ) appear in Terra Sirenum and Terra Cimmeria, regions associated with prominent crustal magnetic anomalies [Acuña et al., 1999].

Localization at degree 50 (Figure 3, top) yields several differences from the results at degree 35 (Figure 3, middle).

**Figure 4.** Gravity/shape admittance and correlation spectra versus spherical harmonic degree  $l$  for Olympus Mons (window center at  $19^\circ\text{N}$ ,  $226.5^\circ\text{E}$ ). Left vertical axis: Solid curves display admittance from observed gravity and shape fields, with formal errors denoted by error bars. Dashed curves show admittances from observed shape and gravity determined from models of thin-spherical-shell flexure with the elastic lithosphere thickness  $T_e$  varying from 0 to 200 km (bottom to top) in 40-km increments, and for a completely uncompensated model (i.e., infinitely rigid lithosphere, infinite  $T_e$ ) for the uppermost curve ('R'). Right vertical axis: Thick solid curves (without error bars) depict correlation between observed gravity and shape fields. Admittance and correlation spectra depend on the spatial localization window. The effects of windows with spectral widths  $L_{win} = 5, 10$ , and 15 are shown from top to bottom panels. Nominal values of model parameters (Table 1) are used for all model admittances.

**Figure 5.** Contours of r.m.s. misfit (mGal/km) between observed and modeled gravity/shape admittances for the Olympus Mons region, for a suite of models with variations in pairs of model parameters. Along the ordinate,  $T_e$  varies in 20-km increments from 0 to 200 km, with the largest value shown corresponding to rigid-lithosphere models (infinite  $T_e$ ). All model parameters are set to nominal values (Table 1) unless otherwise specified.  $L_{win} = 10$ , and the r.m.s. admittance misfit is over the spectral range  $l = 16$  to 50. (a) Tradeoff of  $T_e$  versus  $\rho_l$  (the latter varying in 50-kg/m<sup>3</sup> intervals from 2600 to 3200 kg/m<sup>3</sup>). The best-fitting value for  $\rho_l$  is 2900 kg/m<sup>3</sup>. (b) Tradeoff of  $T_e$  versus  $T_{cr}$ , the latter varying in 10-km increments from 0 to 100 km, for  $\rho_l = 2900$  kg/m<sup>3</sup>. The best-fitting value for  $T_{cr}$  is 0 km. (c) Tradeoff of  $T_e$  versus  $f$  (the latter varying in 0.1-intervals from 0 to 1). The best-fitting value for  $f$  is zero.

Admittances at the Isidis and Argyre basins are less than their values for  $l = 35$ . A broad zone of extremely high admittance ( $> 200$  mGal/km) occurs in the northern lowlands centered approximately at  $72^\circ\text{N}$ ,  $190^\circ\text{E}$ . Correlations south of  $75^\circ\text{S}$  and in several other regions of the southern hemisphere are less (correlation  $< 0.3$ ) than at lower  $l$ . Many regions of the southern highlands show sharply less correlation than at  $l = 35$ , including the south polar region, an area northwest of Hellas, Terra Sirenum, and Terra Cimmeria. Despite these differences, the admittance and correlation highs centered on the Tharsis volcanoes, Elysium rise, and Valles Marineris are robust for all values of  $l$  shown (Figure 3, left).

### 3.2. Admittance and Correlation: Local Spectra

Gravity/shape admittance and correlation spectra for individual regions on Mars provide a means to constrain the regional thickness  $T_e$  of the elastic lithosphere at the time of loading. For each region we consider the sensitivity of model solutions to variations in the parameters  $T_e$ ,  $T_{cr}$ ,  $f$ , and  $\rho_l$ . We restrict our focus to areas with smoothly-varying admittance spectra and correlations near 1; such areas are the most amenable to modeling of the type adopted here. The chosen features and regions include volcanoes, domal rises, prominent troughs, large impact basins, and large expanses of plains; their surface ages span the range of epochs defined for Martian geologic history, from early Noachian to late Amazonian [Tanaka et al., 1992].

**3.2.1. Olympus Mons and Tharsis Montes.** Olympus Mons and the Tharsis Montes are large shield volcanoes with Amazonian-aged surface deposits [Scott and Tanaka, 1986] and prominent free-air gravity anomalies (Figure 3). The admittance spectra for Olympus Mons (Figure 4) are characterized by high magnitudes (generally 100 mGal/km or greater) and prominent upturns in magnitude at short wavelengths (high  $l$ ). Correlations are near 1 over nearly the entire measured wavenumber bands (Figure 4), especially for the spatially narrower windows (larger  $L_{win}$ ). These admittance and correlation spectra are consistent with lithospheric flexure in response to surface loading at high  $T_e$  ( $> 150$  km). The finite-amplitude topography correction to the gravity calculation, in conjunction with the use of the sphere-referenced shape in place of equipotentially-referenced topography, yields rigid-limit (high  $T_e$ ) admittance curves with short-wavelength upturns that match the observed spectra (Figure 4; see also Appendix C). At  $L_{win} = 10$  and 15, there are long-wavelength upturns that have no counterpart in the model admittance curves.

The sensitivity of model solutions at Olympus Mons to variations in model parameters is shown in Figure 5. For variations in  $T_e$  and  $\rho_l$  (Figure 5a), the region of r.m.s. misfit  $< 5$  mGal/km is confined to a zone with  $T_e > 120$  km and  $2800 < \rho_l < 3000$  kg/m<sup>3</sup>. The best-fit model is for essentially a rigid lithosphere with  $\rho_l = 2900$  kg/m<sup>3</sup>. For variations in  $T_e$  and  $T_{cr}$  (and with the best-fit density value from Figure 5a),  $T_e$  decreases slightly as  $T_{cr}$  increases for a given r.m.s. misfit (Figure 5b), demonstrating the well-known tradeoff between these parameters. The shape of the misfit contours indicates that  $T_{cr}$  is not well constrained; any value of  $T_{cr}$  shown can yield a low r.m.s. misfit. However, for likely values of  $T_{cr}$  [50–60 km: Zuber et al., 2000; Zuber, 2001] and r.m.s. misfit  $< 5$  mGal/km,  $T_e > 140$  is required. Further, the lowest r.m.s. misfit values ( $< 3$  mGal/km) occur for  $T_e > 170$  km. Variations in  $T_e$  and  $f$

(Figure 5c), for models with  $z_b = 50$  km, reveal that models with correlated bottom loads ( $f > 0$ ) do not fit well the observed admittance spectrum at Olympus Mons.

Admittance and correlation spectra for the Tharsis Montes volcanoes (Figure 6a) are similar to those observed for Olympus Mons. For  $L_{win} = 5$  windows (not shown), admittance spectra for Ascraeus, Pavonis, and Arsia Montes are very similar. The nominal model parameters (Table 1) yield  $T_e$  estimates of 80–140 km. However, with the more spatially localized  $L_{win} = 15$  windows (Figure 6a), the long-wavelength admittance spectra are consistent with  $T_e$  values  $> 80$  km for Arsia Mons and  $> 160$  km for Pavonis and Ascraeus Montes. Medium-to-short-wavelength admittances can exceed the highest model values shown (Figure 6a). As in Figure 4, correlation spectra in Figure 6a are near unity.

Trade-off studies for model parameters  $T_e$  and  $T_{cr}$  at the Tharsis Montes yield results similar to those for Olympus Mons.  $T_{cr}$  is not constrained. Trade offs of  $T_e$  versus  $\rho_l$ , however, yield preferred density values significantly higher than for Olympus Mons (Figure 6b). The best-fit models are for  $\rho_l = 3050$  kg/m<sup>3</sup> at Ascraeus Mons (Figure 6b),  $\rho_l = 3100$  kg/m<sup>3</sup> at Pavonis Mons and  $\rho_l = 3100$ – $3150$  kg/m<sup>3</sup> at Arsia Mons. For such values of  $\rho_l$ , preferred  $T_e$  values are 70–160 km at Ascraeus Mons, 80–170 km at Pavonis Mons, and 20–70 km at Arsia Mons.

**3.2.2. Alba Patera and Elysium Rise.** Alba Patera is a broad, gently sloped volcano, situated on the northern flank of the Tharsis rise and surfaced with Hesperian to Amazonian volcanic flows [Scott and Tanaka, 1986]. Admittance spectra for Alba Patera demonstrate the utility of the fixed-window approach. For the largest-diameter window ( $L_{win} = 5$ , top of Figure 7), the admittance and correlation spectra somewhat resemble those for the Tharsis Montes: high correlation and admittance magnitudes consistent with  $T_e$  up to 100 km. When localized with smaller windows ( $L_{win} = 10$  or 15), however, the admittance spectra for Alba Patera at long wavelengths ( $l < 36$ ) yield a good match to top-loading flexure models with an elastic lithosphere thickness  $T_e \approx 40$  km (Figure 7, middle and bottom). At shorter wavelengths ( $l > 36$ ), however, the admittance drops sharply, yielding a poor fit to flexure models, but the correlation between gravity and topography falls off as well (Figure 7), so admittances at  $l \geq 36$  are not a basis

**Figure 6.** (a) Gravity/shape admittance and correlation spectra for Tharsis Montes, as in Figure 4, for  $L_{win} = 15$  and nominal model parameter values (Table 1). Top: Ascraeus Mons ( $11.5^\circ\text{N}$ ,  $256^\circ\text{E}$ ). Middle: Pavonis Mons. ( $0.5^\circ\text{N}$ ,  $247^\circ\text{E}$ ). Bottom: Arsia Mons. ( $9^\circ\text{S}$ ,  $239^\circ\text{E}$ ). (b) Contours of r.m.s. admittance misfit (mGal/km) for Ascraeus Mons, as in Figure 5a, for  $T_e$  versus  $\rho_l$ ,  $L_{win} = 15$ , and spectral range  $18 \leq l \leq 45$ .

**Figure 7.** Gravity/shape admittance and correlation spectra for Alba Patera ( $42^\circ\text{N}$ ,  $249^\circ\text{E}$ ), as in Figure 4.

**Figure 8.** Gravity/shape admittance and correlation spectra for (from top to bottom) Alba Patera ( $42^\circ\text{N}$ ,  $249^\circ\text{E}$ ), Ceraunius Fossae ( $30^\circ\text{N}$ ,  $251^\circ\text{E}$ ), and the Elysium rise ( $25^\circ\text{N}$ ,  $147^\circ\text{E}$ ), for  $L_{win} = 10$ .

for distinguishing among models. A trade-off study of the parameters  $T_e$  versus  $\rho_l$  at Alba Patera demonstrates that  $\rho_l$  is unconstrained. A similar study for parameters  $T_e$  and  $f$  indicates that models with  $f < 0.2$  yield acceptable fits to the data; such models exhibit  $T_e$  values up to 60 km.

The Elysium rise volcanic complex consists of a domal rise of height and width very similar to Alba Patera [McGovern *et al.*, 2001] and superposed, relatively steep-sided shield volcanoes (Elysium Mons, Albor Tholus, and Hecates Tholus); surface volcanic units are Hesperian to Amazonian in age [Scott and Tanaka, 1986]. Admittance values for the Elysium rise (Figure 8, bottom) are similar in magnitude to those for Alba Patera at the longest wavelengths shown, but the Elysium admittance values increase faster with increasing  $l$ . Further, short-wavelength admittances at Elysium (Figure 8) approach a rigid limit in contrast to the dropoff seen at Alba Patera, and correlation remains high with increasing  $l$  at Elysium while declining at Alba Patera. Models with  $\rho_l = 3000 \text{ kg/m}^3$  yield the best fit in  $T_e$  versus  $\rho_l$  trade offs, although values in the range  $2900 \leq \rho_l \leq 3050 \text{ kg/m}^3$  yield similar results. Accounting for the possible range in  $\rho_l$ , best-fitting  $T_e$  values at Elysium range from 60 to 90 km.

Admittance curves for the Ceraunius Fossae region south of Alba Patera are consistent with  $T_e = 40\text{--}60 \text{ km}$  for  $L_{win} = 10$  and  $20\text{--}40 \text{ km}$  when more spatially localized at  $L_{win} = 15$  (Figure 8, center). Correlations at Ceraunius Fossae, while generally greater than 0.7, are somewhat lower than at Alba Patera and the Elysium Rise (Figure 8).

**3.2.3. Highland Plana.** The Thaumasia Plateau region of southeastern Tharsis consists of broad volcanic plains (Syria, Solis, and Sinai Plana) ringed by rugged highlands (Claritas Fossae, the Thaumasia highlands, and the Coprates rise); these units are mostly of Noachian and Hesperian age [Dohm and Tanaka, 1999]. Solis Planum, for  $L_{win} = 5$  and  $10$ , exhibits admittance spectra of intermediate magnitude, with generally high correlations (Figure 9). For  $L_{win} = 10$ , the admittance spectrum is consistent with purely surface-loaded models at low  $T_e$  (20–35 km). For  $L_{win} = 15$ , the correlations are significantly reduced compared with the other two windows. Syria Planum (not shown) exhibits a pattern similar to that for Solis Planum, except that admittance spectra for  $L_{win} = 5$  and  $10$  are substantially higher in magnitude than those in Figure 9, most likely due to proximity to the strong gravity signal of the Tharsis Montes.

**3.2.4. Valles Marineris.** Admittance and correlation spectra for the different parts of the Valles Marineris chasm system tend to exhibit similar features. In Candor Chasma,

**Figure 9.** Gravity/shape admittance and correlation spectra for Solis Planum ( $25^\circ\text{S}$ ,  $270^\circ\text{E}$ ), as in Figure 4.

**Figure 10.** (a) Gravity/shape admittance and correlation spectra with  $L_{win} = 15$ , for eastern Candor Chasma ( $8^\circ\text{S}$ ,  $295^\circ\text{E}$ ) in Valles Marineris. Top: nominal models. Middle: low-surface-density models ( $\rho_s = 2000 \text{ kg/m}^3$ ). Bottom: models with  $f = 0.5$  and nominal surface density ( $2900 \text{ kg/m}^3$ ). (b) Contours of r.m.s. admittance misfit (mGal/km) at Candor Chasma, as in Figure 5, for  $T_e$  versus  $\rho_s$ ,  $L_{win} = 15$ , and spectral range  $18 \leq l \leq 45$ . (c) As in Figure 10b, for  $T_e$  versus  $f$ .

the admittance spectrum is flat and is not fit well by the nominal model with any particular value of  $T_e$  (Figure 10a, top). The correlation is nearly unity at all but the longest wavelengths. The flatness of the admittance spectrum suggests a largely uncompensated model, but with a lower magnitude than for the nominal (top-loaded) rigid-limit model. A satisfactory admittance match across the modeled waveband can be accomplished in two ways: a large reduction in surface density  $\rho_s$  ( $\rho_s = \rho_l = \rho_c = 2000 \text{ kg/m}^3$ ; Figure 10a, center), or a significant component of subsurface loading ( $f > 0.5$ ; Figure 10a, bottom). For the latter model, the mass deficit of the trough is partially compensated by a dense (density contrast  $\rho_b = 600 \text{ kg/m}^3$ ) subsurface load at depth  $z_b$ ; for this particular model  $z_b$  is set equal to the  $T_{cr}$  value of 50 km, corresponding to the crust-mantle boundary. Compensation increases (and admittance magnitude decreases) with increasing  $f$  such that as  $f$  approaches unity, the admittance spectrum for any  $T_e$  converges to that for conventional Airy isostasy ( $f = 1$  and  $T_e = 0$ ).

The relationship between model parameters  $T_e$  and  $\rho_s$  at Candor Chasma is demonstrated in Figure 10b, for a model suite with  $f = 0$ . The best-fit models are confined to a narrow density range ( $1900\text{--}2100 \text{ kg/m}^3$ ) and to  $T_e \geq 100 \text{ km}$ . A similar study for parameters  $T_e$  and  $f$  with  $\rho_s = 2900 \text{ kg/m}^3$  (Figure 10c) reveals a narrow range for  $f$ , centered on the value 0.6, and  $T_e > 150 \text{ km}$ . Model parameters  $\rho_s$  and  $f$  trade off with each other such that, as one increases, the value of the other required to fit a given observed admittance spectrum also increases. Thus, successful models occur for low (Figure 10a, middle) or high (Figure 10a, bottom) values of these quantities.

Admittance spectra for Capri and Hebes Chasmata, respectively east and west of Candor Chasma, are qualitatively similar to those in Figure 10a; nearly flat spectra that are poorly matched by the nominal surface-loading models. Compared with Candor Chasma, admittance magnitudes at Capri Chasma are somewhat higher and those at Hebes Chasma are somewhat lower. On the basis of the model suite shown in Figure 10b ( $f = 0$ ), the best-fit range of  $T_e$  is  $60\text{--}130 \text{ km}$  for  $\rho_s = 1900\text{--}2300 \text{ kg/m}^3$  at Hebes Chasma and  $\geq 120 \text{ km}$  for  $\rho_s = 2400$  at Capri Chasma. For models with bottom loading (model suite of Figure 10c),  $T_e \geq 80 \text{ km}$  for  $f = 0.6\text{--}0.8$  at Capri Chasma and  $T_e \geq 120 \text{ km}$  for  $f = 0.3\text{--}0.4$  at Capri Chasma. Correlations in Valles Marineris are generally very high, except for a decline at low  $l$  which is almost negligible at Capri Chasma (easternmost), noticeable at Candor Chasma (Figure 10a), and prominent at Hebes Chasma (westernmost).

**3.2.5. Impact Basins.** The Hellas, Argyre, and Isidis basins are presumed to have been excavated by large impact events early in Martian history. The presence of a fourth large basin in Utopia Planitia, initially proposed on geological grounds [McGill, 1989], was confirmed by MGS topography data [Smith *et al.*, 1999a]. The Hellas basin, the largest in diameter and deepest (9 km) on Mars, is surrounded by an annulus of elevated topography that may be composed of ejecta from the basin-forming impact [Smith *et al.*, 1999a]. If so, the ejecta constitute a substantial surface

**Figure 11.** Gravity/shape admittance and correlation spectra, as in Figure 4, for the (a) Hellas ( $42^\circ\text{S}$ ,  $66^\circ\text{E}$ ), and (b) Isidis ( $12^\circ\text{N}$ ,  $87^\circ\text{E}$ ) basins.

load on the lithosphere. The Isidis basin exhibits a particularly strong positive gravity anomaly (Figure 1c); such an anomaly, when associated with a topographic low, is analogous to a lunar “mascon.” Mascons indicate a subsurface mass excess that loads the lithosphere. Important contributions to mascon loads come from superisostatic uplift of the crust-mantle boundary beneath the basin [Neumann *et al.*, 1996; Wieczorek and Phillips, 1999] and infilling of the basins by sediments (as at Argyre) or volcanic material (as at Isidis; see Comer *et al.* [1985]; Head *et al.* [2002]). Such infilling, carried more nearly to completion, has also been proposed to account for the gravity anomaly over the Utopia basin [Smith *et al.*, 1999b; Zuber *et al.*, 2000].

Admittance spectra at the Hellas basin (Figure 11a) have low magnitudes, generally consistent with  $T_e < 10$  km. Correlation spectra exhibit significant lows at long and intermediate wavelengths for each window shown. The magnitude of the correlation drop increases with increasing  $L_{win}$ ; for  $L_{win} = 15$ , correlations drop below zero at degrees 19 and 28–30 (Figure 11a). Trade-off studies of model parameters  $T_e$  and  $T_{cr}$  at Hellas (performed with  $L_{win} = 5$ , a window wide enough to resolve the entire basin) yield a strong fit to  $T_{cr} = 50$  km and  $T_e < 10$  km. Trade-off analysis of  $T_e$  and  $\rho_s$  at Hellas indicates that no particular value of density is strongly favored. Similar studies of  $T_e$  and  $f$  yield a solution branch with  $f \approx 1$  and any value for  $T_e$ ; however, this outcome is likely a consequence of the convergence of all admittance curves (for any  $T_e$ ) to the Airy ( $T_e = 0$ ) curve as  $f$  approaches 1 (for the type of bottom loading modeled here).

At the Isidis basin (Figure 11b), admittance and correlation spectra provide poor matches to the flexure models. Both admittances and correlations tend to be negative at long wavelengths and positive at short wavelengths. For a given  $L_{win}$ , the transition from negative to positive occurs at similar  $l$  for both admittance and correlation. The magnitude of the negative and positive extrema increases with increasing  $L_{win}$ . At the Argyre basin, admittance and correlation spectra are similar to those seen at Isidis. However, at Argyre the range of admittance values is lower, and the transition from negative to positive admittance and correlation occurs at higher  $l$  than at Isidis.

On the western rim of the Hellas basin, admittance spectra (Figure 12a) are similar to those localized within the basin (Figure 11a), indicating that  $T_e$  lies in the range 0–15 km. A trade-off study of  $T_e$  and  $T_{cr}$  for the western rim of Hellas (Figure 12b) indicates that  $T_e$  decreases as  $T_{cr}$  increases for a given misfit. The best fit (for  $L_{win} = 15$ ) occurs for a model with  $T_e = 5$  km and  $T_{cr} = 50$  km.

Low admittance values, consistent with thin lithosphere, are also seen on the southern rim of Hellas for the largest-diameter spatial window ( $L_{win} = 5$ ; top of Figure 12c). However, admittance magnitudes increase with increasing spatial localization, requiring increased  $T_e$  or  $T_{cr}$  to fit observations. A  $T_e$ - $T_{cr}$  trade-off study (Figure 12d) finds solutions with high misfits at moderate  $T_e$ . Better fits are

**Figure 12.** (a) Gravity/shape admittance and correlation spectra for the western Hellas rim (42°S, 39°E). (b) Contours of r.m.s. admittance misfit (mGal/km) at the western Hellas rim, as in Figure 5, for  $T_e$  versus  $T_{cr}$ ,  $L_{win} = 15$ , and spectral range  $18 \leq l \leq 45$ . (c) As in (a), for the southern Hellas rim (64°S, 66°E). (d) As in (b), for the southern Hellas rim. (e) As in (d), for the southern Hellas rim and  $T_e$  versus  $f$ .

found for higher reference crustal thicknesses, with the best fit occurring at the highest  $T_{cr}$  shown (100 km) and  $T_e = 10$  km. The average crustal thickness for the Hellas region is unlikely to be as great as 100 km, however, on the basis of the argument that temperatures near the base of such thick crust would lower the effective viscosity to the point that lower crustal flow would remove lateral variations in crustal thickness [Zuber *et al.*, 2000; Nimmo and Stevenson, 2001]. On the other hand, the globally averaged value for  $T_{cr}$  is unlikely to be significantly less than 50 km, lest modeling of lateral variations in crustal thickness from observed gravity and topography predict negative values for thickness [Zuber *et al.*, 2000].

Accepting the best-fitting values of  $T_{cr}$  (50–60 km) from Zuber *et al.* [2000], we explore the possibility that subsurface loading contributed to the observed admittance spectrum at the southern rim of Hellas. For a suite of models with subsurface loading at the crust-mantle boundary (Figure 12e), best-fit solutions exist for a bottom load fraction  $f = 0.3$  to 0.6 and  $60 \leq T_e \leq 200$  km, with a best fit at  $f = 0.4$ ,  $T_e = 80$  km. However, trade-off studies for  $T_e$  and  $\rho_s$  yield best-fit models with  $\rho_s \leq 2700$  kg/m<sup>3</sup> and  $T_e \geq 40$  km.

**3.2.6. Southern Uplands.** In the ancient southern highlands, low admittance magnitudes and intermediate to high correlations are characteristic. At Noachis Terra, the type terrain for the Noachian epoch, admittance magnitudes are consistent with nearly complete local (Airy) compensation of topography for  $L_{win} = 10$  (Figure 13a, top) and 15. The observed admittance falls slightly below the Airy ( $T_e = 0$ ) curve for the shortest wavelengths; correlation also declines at high  $l$ . At Terra Cimmeria (Figure 13a, middle) admittance curves at high  $l$  tend to fall well short of the Airy curves, and increasingly so with increasing  $L_{win}$ . Correlation spectra at Terra Cimmeria are generally similar to those at Noachis Terra. Admittance spectra at Terra Sirenum (Figure 13a, bottom) also exhibit a strong short-wavelength divergence from the Airy curves, but correlations can be significantly lower than for other southern highland regions (e.g., Figure 13a, top and middle), near 0.5 for large portions of the spectra. Trade-off studies of model parameters  $T_e$  and  $T_{cr}$  at Noachis Terra reveal that solutions with  $T_e$  as large as 15 km give acceptable fits to the observed admittance (Figure 13b). Similar trade-off studies of  $T_e$  and  $\rho_s$  suggest that load and crustal densities of 2700 kg/m<sup>3</sup> yield the best admittance fit (at  $T_e = 0$  km).

**3.2.7. Northern Lowlands.** The admittance and correlation spectra for the northern lowlands display large variations in admittance magnitude, high formal errors in admittance, and frequent negative-to-positive (and vice-versa) swings in correlation. No surface loading model, even with bottom loading, provides a good fit to the observed admittance and correlation.

## 4. Discussion

### 4.1. Regional Analysis

**4.1.1. Olympus Mons and Tharsis Montes.** The gravity/shape admittance and correlation spectra for Olym-

**Figure 13.** (a) Gravity/shape admittance and correlation spectra for the southern highlands; (top) Noachis Terra (35°S, 26°E); (middle) western Terra Cimmeria (45°S, 150°E); (bottom) Terra Sirenum (60°S, 240°E). (b) Contours of r.m.s. admittance misfit (mGal/km) for Noachis Terra, as in Figure 5, for  $T_e$  versus  $T_{cr}$ , with  $\rho_s = 2700$  kg/m<sup>3</sup> (the best-fit density from a tradeoff of  $T_e$  and  $\rho_s$ ),  $L_{win} = 15$ , and spectral range  $18 \leq l \leq 45$ .



pus Mons and the Tharsis Montes (Figures 4–6) are generally consistent with simple models of lithospheric flexure in response to volcanic surface loads. In contrast, earlier studies that employed the mass-sheet approximation in gravity models were unable to match observed admittance magnitudes, particularly at short wavelengths (see Appendix C), without invoking extremely large densities [McGovern *et al.*, 2000] or dense buried loads [Arkani-Hamed, 2000]. When gravity models for the central Tharsis region are calculated with the finite-amplitude formalism, however, the resulting medium- to short-wavelength admittance spectra match observed spectra without any need to invoke extraordinary loads.

The admittance spectra nonetheless suggest modest departures from the nominal model presented here. For example, the nominal load density ( $2900 \text{ kg/m}^3$ ; Table 1) is exceeded at Ascræus Mons (best fit value of  $3050 \text{ kg/m}^3$ ), Pavonis Mons ( $3100 \text{ kg/m}^3$ ), and Arsia Mons ( $3100\text{--}3150 \text{ kg/m}^3$ ). That higher density values appear to be favored for the Tharsis Montes could indicate the emplacement of more mafic or less vesicular volcanic material, or a greater ratio of intrusive to extrusive material, at these edifices than in other regions. McKenzie *et al.* [2002] found similarly high densities ( $3000 \text{ kg/m}^3$ ) for the Tharsis region.

The elastic lithosphere thickness values for Olympus Mons, Ascræus Mons, and Pavonis Mons are all generally higher than the value for Tharsis as a whole (70 km) found by McKenzie *et al.* [2002] (the  $T_e$  range for Arsia Mons includes the latter value). Differences in localization likely account for the disparity. The cartesian area used by McKenzie *et al.* [2002] to isolate Tharsis extends over  $50^\circ\text{S}$  to  $50^\circ\text{N}$  and  $195^\circ$  to  $285^\circ\text{E}$ . Such a region encloses a variety of geologic structures, formed at various times by different processes. Harmonic analysis on a grid will inevitably mix the signals from all such structures. Since the provinces with greatest relief dominate the admittance signal [Forsyth, 1985], the “Tharsis” signal seen by McKenzie *et al.* [2002] will be dominated by the high-magnitude (high- $T_e$ ) signal from the large shield volcanoes. These strong signals will nonetheless be diluted by signals of much lower magnitude from the remainder of the box area (see Figure 3). The resulting  $T_e$  value will underestimate the actual values at Tharsis Montes but may overestimate the  $T_e$  corresponding to the formation of the Tharsis rise as a whole (that is, under the questionable assumption that the entire Tharsis rise formed under a single, uniform set of conditions). In contrast, the narrower windows used here allow isolation of individual components of the Tharsis rise, for example, the shield volcanoes surfaced with Amazonian flows (Figures 4–6), the broad volcanic domes having Amazonian and Hesperian surface units (e.g., Alba Patera, Figures 7, 8, and Syria Planum), and densely fractured Noachian terrain (Ceraunius Fossae, Figure 8). The  $T_e$  estimate of McKenzie *et al.* [2002] is therefore not likely to represent the condition governing the formation of the Tharsis rise, but instead is an average weighted by the characteristic admittance magnitudes and areal extents of the individual components of Tharsis and other regions in the included area.

**4.1.2. Alba Patera and Elysium Rise.** Localized admittance spectra at Alba Patera yield an excellent fit to  $T_e = 40\text{--}60$  km. This result is consistent with estimates for  $T_e$  from a sill-inflation model for the construction of the edifice [McGovern *et al.*, 2001], constrained by the surficial distribution of tectonic features on Alba Patera. The correlation and admittance dropoffs at high  $l$  may indicate short-wavelength intra- and sub-crustal intrusions that are uncorrelated with current topography [McGovern *et al.*, 2001].

Admittance and coherence spectra for the Elysium rise (Figure 8) resemble those for Alba Patera (Figure 7) at long

wavelengths, but at shorter wavelengths they resemble those for the Tharsis Montes and Olympus Mons (Figures 4, 6a). We suggest that the long-wavelength structures of Alba Patera and the Elysium rise are similar and that the two features may be grouped under the category “domal rises.” The short-wavelength admittance and correlation at Elysium rise are dominated by the large volcanoes atop the rise, analogous to the Tharsis Montes shields. In contrast, the summit edifice at Alba does not obscure the short-wavelength signal from intrusive loading that is uncorrelated with surface relief (Figure 7). Thus, while the Elysium rise and Alba Patera may have shared a common history of formation by combined surface and intrusive loading [e.g., the scenario of McGovern *et al.* 2001], they experienced distinct near-summit activity in their most recent stages of evolution. The best-fitting values for  $T_e$  for the Elysium rise (50–80 km) are similar to or slightly greater than for Alba Patera.

As at the Tharsis Montes, the  $T_e$  estimate for Elysium by McKenzie *et al.* [2002] (29 km) is substantially lower than the range found here (50–80 km). Again, it is likely that averaging of the admittance signal from the target (the Elysium rise) with that of other regions within the very large cartesian area ( $10^\circ\text{S}$  to  $60^\circ\text{N}$ ,  $115^\circ$  to  $175^\circ\text{E}$ ) used by McKenzie *et al.* [2002] results in an underestimate of the true  $T_e$  value for the rise.

As noted in the previous section, solutions for  $T_e$  at Arsia Mons admit to smaller values than those indicated for the other Tharsis Montes and Olympus Mons, and the values overlap those determined for the domal rises (Elysium rise in particular). This finding permits scenarios in which the evolution of Arsia Mons followed a path similar to those of Alba Patera and the Elysium rise. Arsia Mons has several physical features in common with these structures, including annular extensional faulting and domical topography. The faults have been linked to intrusion processes [Scott and Wilson, 1999; Montési, 2001] in a manner similar to the intrusion-based scenario of McGovern *et al.* [2001] for the construction of domal rises. Alternatively, Arsia Mons may have been emplaced atop an older structure (perhaps an ancient domal rise [e.g., Dohm *et al.*, 2001] or edifice [e.g., Webb *et al.*, 2001]) that was itself built on lithosphere with moderate  $T_e$ , and the gravity/topography signal from this structure has not been completely obscured by the Arsia Mons edifice.

**4.1.3. Highland Plana.** Syria and Solis Plana exhibit admittance spectra generally consistent with low  $T_e$  (20–50 km) at the time of formation (e.g., Figure 9, center). However, relatively low correlations found for the spatially narrowest windows (e.g., Figure 9, bottom) suggest the presence of significant (but local) subsurface loads. Such regions, with surfaces Noachian to Hesperian in age, were not subsequently mantled by Amazonian deposits, as was the central Tharsis region. We suggest that the gravity/topography relationships seen at Syria and Solis Plana may have been typical for the Tharsis region during the Hesperian epoch; elsewhere in Tharsis, such signals have since been obscured by those representative of younger volcanic structures. However, we note that solutions with higher  $T_e$  are allowable in the presence of significant subsurface loads.

**4.1.4. Valles Marineris.** Admittance and correlation spectra for Valles Marineris are flat or nearly so over the entire waveband (e.g., Figure 10a), suggesting that the troughs are relatively uncompensated. Solely surface-loaded models require very low material density ( $< 2400 \text{ kg/m}^3$ , e.g., Figure 10a, middle, Figure 10b) to match the admittance magnitude. *McKenzie et al.* [2002] also inferred relatively low values of crustal density ( $2300 \text{ kg/m}^3$ ) at Valles Marineris (for the region enclosed by  $35^\circ\text{S}$  to  $25^\circ\text{N}$ ,  $260^\circ$  to  $350^\circ\text{E}$ ). Such low densities are not consistent with unaltered basaltic lava flows [*McEwen et al.*, 1999], but might be consistent with compacted sedimentary or ash deposits, making up the layers that outcrop in the walls of the Valles Marineris chasms. Other possibilities include hydrothermal alteration and dissolution of originally denser basaltic material, or the presence of interstitial ice [e.g., *McKenzie et al.*, 2002]. For Hebes Chasma and Candor Chasma, we find that models lacking subsurface loading require crustal densities even lower ( $\approx 2000\text{--}2200 \text{ kg/m}^3$ ) than found by *McKenzie et al.* [2002] to fit the observed admittance spectra. Given the abundant evidence for emplacement of basaltic (i.e., relatively dense) material in the highland plateaus surrounding Valles Marineris and arguments for a volcanic origin for the layered deposits exposed in the chasm walls [*McEwen et al.*, 1999], such an extremely low density for the local crust is unlikely. Nonetheless, if a low-density, purely surface-loaded scenario holds, the admittance spectra still require  $T_e$  to be significantly larger ( $\geq 80 \text{ km}$ ) than the  $53 \text{ km}$  found by *McKenzie et al.* [2002]. Once again, the difference is likely due to the averaging of signals over the large area used by *McKenzie et al.* [2002] for investigating Valles Marineris. The localization windows used here allow us to isolate the characteristic spectra of individual sections of the Valles Marineris system.

Both the relative flatness and the magnitudes of admittance spectra at Valles Marineris sites are also fit well by models with the nominal crustal density ( $2900 \text{ kg/m}^3$ , Table 1) and a significant component of subsurface loading at the crust-mantle boundary ( $f \geq 0.3$ , Figures 10b-10d). The subsurface loads, correlated with the surface topography by assumption, partially compensate the trough mass deficit such that admittance magnitude is reduced. Plausible mechanisms for forming such subsurface loads include rift-induced crustal thinning and intrusion of high-density dikes beneath the troughs. However, the classical rifting mechanism for formation of Valles Marineris troughs is not favored by the gravity and topography fields returned by MGS, for two reasons. First, no plausible solutions with  $T_e < 80 \text{ km}$  were found, even allowing for wide variations in surface density and subsurface loading. Given that rifting is favored by low lithospheric rigidity (i.e., low  $T_e$ , at least locally), it is unlikely that rift-induced relief would exhibit the admittance spectra observed at Valles Marineris. The absence of topographic evidence for uplifted fault flanks [*Schultz and Lin*, 2001] also argues against the sort of scenario (high heat flux, locally low  $T_e$ ) typically associated with rifting.

A scenario for Valles Marineris trough formation consistent with the observed gravity/topography relationships is that dense mafic dikes emplaced in the lower crust partially compensate the troughs of Valles Marineris. [cf. *Mège and Masson*, 1996 a,b; *McKenzie and Nimmo*, 1999; *Ernst et al.* 2001]. These intrusive bodies load a comparatively thick elastic lithosphere ( $T_e \geq 80 \text{ km}$ ) and could account for the relative flatness of the admittance spectra and the absence

of uplifted chasm flanks that would be predicted by a low- $T_e$  rifting mechanism. These dikes may intrude crust of somewhat lesser density than the nominal  $2900 \text{ kg/m}^3$  value from Table 1; the lower the crustal density, the lower the amount of intrusive material required. The dikes would likely propagate laterally from a magma source in the central Tharsis region. Syria Planum in particular has been identified as a magmatic center of major significance in the Hesperian [*Tanaka and Davis*, 1988; *Mège and Masson*, 1996a,b; *Webb et al.*, 2001]. The degree of subsurface loading  $f$  in the models presented above likely scales with the intensity of diking. If so, the decrease of inferred  $f$  with distance from Tharsis (i.e., from Hebes to Candor to Capri Chasmata, Figures 10c-e) is consistent with dike intensity decreasing with distance from a magma source in central Tharsis. Under this scenario, the Valles Marineris troughs formed by a combination of collapse and extensional faulting. Trough boundaries are strongly influenced by fault orientations, which in turn are controlled by dike-induced extension (approximately north-south) in the near-surface rocks.

**4.1.5. Impact Basins.** The Hellas basin region (Figure 11a) has characteristically low admittance for all windows considered here, with  $T_e$  ranging from 0 to  $10 \text{ km}$ . This result is consistent with Airy isostasy, as concluded by *Smith et al.* [1999], *Zuber et al.* [2000], and *Turcotte et al.* [2002]. Similar results are seen on the western rim of the basin (Figure 12a). However, the admittance on the southern rim of Hellas increases with increasing spatial localization (Figure 12c). For purely surface-loaded models (see also Figure 12d), a value for  $T_e$  of up to  $25 \text{ km}$  is indicated. If a  $T_e \approx 20 \text{ km}$  solution is adopted, the admittance can be interpreted as the surface loading signal of the Peneus Patera and Amphitrites Patera volcanoes. Their flanks are of early Hesperian age and consist of ridged plains and dissected units [*Tanaka and Scott*, 1987] with extremely low slopes. The high value for  $T_{cr}$  ( $100 \text{ km}$ ) found for the best-fit flexure model at the southern rim of Hellas is less straightforward to interpret. Globally-constrained estimates of crustal thickness [e.g., *Zuber et al.*, 2000; *Zuber*, 2001] in this region show no unusual crustal thickening at southern Hellas relative to other locations in the southern hemisphere. Further, topographic relaxation arguments suggest that values of  $T_{cr} > 100 \text{ km}$  are unlikely [*Zuber et al.*, 2000; *Nimmo and Stevenson*, 2001]. However, subsurface loading models with lower values for  $T_{cr}$  [ $50 \text{ km}$ , *Zuber et al.*, 2000; *Zuber*, 2001] yield well-constrained values for  $T_e$  ( $100\text{--}200 \text{ km}$ , best fit  $120 \text{ km}$ ) and  $f$  ( $0.5\text{--}0.6$ , best fit  $0.5$ ). Such results may reflect magmatic intrusive loading associated with the Hesperian volcanoes discussed above. Low gravity/shape correlations elsewhere on the rim of Hellas (e.g., the low-correlation area northeast of Hellas in Figure 3) hinder estimation of  $T_e$  with the methods described here.

The transitions from negative to positive admittance and correlation with increasing  $l$  observed at Argyre and Isidis (Figures 3, 11b) reflect the presence of subsurface mass anomalies (mascons). In contrast, for Hellas the admittance and correlation near  $l = 30$  for  $L_{win} = 15$  (Figure 11a) suggest only a weak mascon of much smaller extent than the basin itself. At long wavelengths (low  $l$ ), the positive gravity anomaly from the Argyre and Isidis mascons interacts with the negative relief of the basin to produce negative admittance and correlation spectra. Thus, the degree at which the positive-to-negative transition occurs is likely controlled

by the horizontal extent of the anomalous mass and basin. At wavelengths shorter than the characteristic dimensions of the mascon and basin, admittance and correlation values become positive (Figure 11b). At such wavelengths, one would expect that a surface loading signal would dominate, and therefore that surface-loaded flexure models would be useful. At Isidis, however, short-wavelength admittance magnitudes are well in excess of those predicted by surface-loaded flexure models (Figure 11b). This tendency toward extremely high positive admittances increases with increasing spatial localization (increasing  $L_{win}$ , Figure 11b). The elevated short-wavelength admittances are likely due to some combination of subsurface loads positively correlated with topography and the effect of window widths that become comparable with the diameters of the basin and mascon load.

**4.1.6. Southern Uplands.** Admittance and correlation spectra for the ancient (generally Noachian-age surface) southern highlands of Mars tend to fall into two categories. In both categories, admittance spectra have low magnitudes and low formal errors. The first category, illustrated by Noachis Terra (Figure 13a, top), exhibits moderate to high correlation (for the most part greater than 0.7) and admittance broadly consistent with compensation by Airy isostasy or small  $T_e$  ( $< 15$  km, Figure 13b). Similar spectral behavior is seen elsewhere in Noachis Terra and in northeastern Arabia Terra ( $36^\circ\text{N}$ ,  $40^\circ\text{E}$ ) and northeastern Terra Cimmeria ( $30^\circ\text{S}$ ,  $180^\circ\text{E}$ ). The  $T_e$  results in such areas are similar to that obtained by *McKenzie et al.* [2002] for the southern hemisphere as a whole. The second category, illustrated by western Terra Cimmeria ( $45^\circ\text{S}$ ,  $150^\circ\text{E}$ ; Figure 13a, middle) and Terra Sirenum (Figure 13a, bottom), is characterized by admittance spectra that are near the Airy curve at low  $l$  but fall significantly below that curve at high  $l$ . Such behavior is also seen in parts of Arabia Terra and to a lesser extent in Noachis Terra and Terra Meridiani. Correlation spectra in these regions can range from moderately high (generally  $\geq 0.7$ , Figure 13a, top and middle) to intermediate (often  $< 0.7$ , Figure 13a, bottom). Most parts of Terra Cimmeria and Terra Sirenum exhibit the short-wavelength admittance falloff seen in Figure 13a. These regions are the sites of the largest-amplitude crustal magnetic sources detected by the MGS magnetometer experiment [e.g., *Acuña et al.*, 1999]. The correlation and admittance spectra shown in Figure 13a for western Terra Cimmeria and particularly for Terra Sirenum are suggestive of a subsurface load component uncorrelated with the surface relief. These observations are consistent with scenarios in which the anomalous magnetizations arise from crustal intrusions [e.g., *Connerney et al.*, 1999; *Nimmo*, 2000].

Several regions in the cratered uplands of Mars are distinguished by unusually low gravity/shape correlations, including central Arabia Terra, Tempe Terra, and an area northeast of the Hellas basin (Figure 3, right). *Hynek and Phillips* [2001] describe geologic, topographic, and stratigraphic evidence for widespread erosion in the cratered terrain of Arabia Terra during the late Noachian. Erosion is known to cause decorrelation of gravity and topography [e.g., *Forsyth*, 1985]; this outcome is also possible at Arabia Terra if components of shape that were originally correlated with gravity were frozen in before most erosion occurred (i.e., before the late Noachian). Intrusive volcanism and erosion of surface volcanic deposits associated with Hadriaca and Tyrrhena Paterae [e.g., *Crown and Greeley*, 1993] could account for the decorrelation of gravity and shape to the northwest of Hellas. However, the admittance and correlation pattern

in this region (negative at long wavelengths and positive at short wavelengths) is also consistent with the “mascon” pattern seen at the Isidis and Argyre basins (Figure 11b). Thus, an alternative explanation for the anomaly to the northeast of the Hellas basin is a mascon basin buried by Hellas ejecta, perhaps corresponding to the “south Hesperia basin” postulated by *Schultz and Frey* [1990].

**4.1.7. Northern Lowlands.** The large fluctuations of admittance and correlation spectra in the northern lowlands of Mars likely reflect subsurface loads that are uncorrelated with the extremely smooth topography of the northern lowlands. The present lowland surface is the product of the deposition of Hesperian-aged ridged plains of probable volcanic origin [*Head et al.*, 2002] and the later emplacement of the Amazonian Vastitas Borealis Formation. The low power in the topography (shape) spectrum relative to the gravity signal accounts for the wide range of admittance values seen. Much of this behavior is likely related to buried impact basins, such as the Utopia basin [*Zuber et al.*, 2000] and a number of other probable impact features barely discernible in the present topography [*Frey et al.*, 2001]. Further, several linear negative gravity anomalies to the northeast of the Tharsis rise (also in a zone of low gravity/topography correlation, see Figure 3) have been attributed to the formation of fluvial channels that were later filled with low-density sediments [*Phillips et al.*, 2001]. The simple lithospheric loading models presented here are not well suited for modeling the admittance and correlation spectra for regions with the characteristics of the northern lowlands. More detailed forward models of the gravity field predicted by specific subsurface loads are required to yield constraints on the nature of the lithosphere in this area.

## 4.2. Thermal History of Mars

We may apply our estimates of elastic lithosphere thickness  $T_e$  to elucidate the thermal history of Mars. For each region or feature discussed above we convert  $T_e$  to estimates of mean lithospheric thermal gradient  $\frac{\partial T}{\partial z}$  and heat flux  $q$ . We then compare our results with those of previous workers and evaluate trends with respect to the age of each feature. A summary of our findings is given in Table 3.

We convert  $T_e$  to  $\frac{\partial T}{\partial z}$  using the strength envelope formalism of *McNutt* [1984]. The heat flux  $q$  can then be estimated from  $q = k \frac{\partial T}{\partial z}$ , where  $k$  is the mean thermal conductivity, appropriately weighted for the proportion of crust ( $k = 2.5$  W m $^{-1}$  K $^{-1}$ ) and mantle ( $k = 4.0$  W m $^{-1}$  K $^{-1}$ ) in the lithosphere. The thermal gradient is estimated by determining the thickness  $T_m$  of an elastic-plastic plate with the

**Figure 14.** Lithospheric thermal gradient  $dT/dz$  (in K/km) and heat flux  $q$  (in mW/m $^2$ ) versus surface age for several regions on Mars. Three of the age subdivisions correspond to the Noachian, Hesperian, and Amazonian epochs (in order of decreasing age); the remaining two are used to identify features that exhibit surface unit ages spanning two epochs (see also Table 3). Within a given age subdivision, vertical positions give an approximate indication of the relative surface ages of features, based on crater counts [e.g., *Plescia and Saunders*, 1979; *Neukum and Hiller*, 1981] and geologic mapping [e.g., *Scott and Tanaka*, 1986; *Greeley and Guest*, 1987], although the development of a given pair of features may have overlapped in time. (a) Lithospheric thermal gradients based on  $T_e$  estimates in this paper. (b) Heat fluxes based on  $T_e$  estimates in this paper.

same bending moment and curvature as the elastic plate of thickness  $T_e$  [McNutt, 1984]. The mechanical lithosphere thickness,  $T_m$ , is always equal to or greater than  $T_e$ , by an amount that increases with increasing plate curvature. The conversion to  $T_m$  requires assumptions regarding the strain rate, rock friction law, and ductile strength of the lithosphere. This conversion can be expressed in graphical form as a chart: given  $T_e$  and plate curvature,  $T_m$  and  $\frac{\partial T}{\partial z}$  can be read from the chart. We use charts of the type shown in Figures 5 and 6 of *Solomon and Head* [1990]. The low-pressure friction law of *Byerlee* [1978] defines the brittle portion of the strength envelope; the ductile portion is given by flow laws for olivine [Goetze, 1978; Evans and Goetze, 1979] and diabase [Caristan, 1982], respectively. We assume strain rates between  $10^{-19}$  and  $10^{-16}$  s $^{-1}$ , corresponding to the accumulation of 1% strain in 3 billion and 3 million years, respectively. Crustal thickness is assumed to be 50 km [Table 1; Zuber et al., 2000; Zuber, 2001]. For regions with  $T_e$  comparable to this value, we calculate  $\frac{\partial T}{\partial z}$  and  $q$  for both olivine and diabase flow laws. Plate curvature is calculated directly from the second derivative of modeled lithospheric deflections, for models with the bounding values of  $T_e$  for each feature (Table 3, third column). We use the maximum curvature associated with a given feature [e.g., McNutt, 1984]. *Solomon and Head* [1990] discussed the uncertainties involved in this procedure.

Our results are shown in Figure 14. The five subdivisions of the vertical axes in Figure 14 indicate the approximate surface age of a load feature, as given in the second column of Table 3. The horizontal axes in Figure 14 give the thermal gradient  $\frac{\partial T}{\partial z}$  (Figure 14a) and heat flux  $q$  (Figure 14b). A horizontal bar delimits the range of  $\frac{\partial T}{\partial z}$  and  $q$  for each feature or region. Arrows at the end of a bar indicate the absence of an upper bound for the relevant parameter.

The Noachian cratered southern highlands and Hellas Basin exhibit the largest thermal gradient and heat flux magnitudes of our study areas. Possible solutions for the south Hellas rim volcanoes (Noachian and Hesperian in age) include both low ( $\frac{\partial T}{\partial z} = 3.5\text{--}11$  mW/m $^2$ ) and high ( $\frac{\partial T}{\partial z} > 9$  mW/m $^2$ ) thermal gradient branches; the former invokes intrusive loading that may be significantly different in age from the surface units. Hesperian highland plana yield intermediate estimates of  $q$  and  $\frac{\partial T}{\partial z}$ , as do Hesperian-Amazonian domal rises. Lithospheric thermal gradients and heat fluxes for Hesperian-Amazonian Valles Marineris and shield volcanoes with Amazonian surface ages are generally  $< 9$  K/km and  $< 28$  mW/m $^2$ , respectively. Given the association of magmatism with positive thermal anomalies, local estimates of  $q$  and  $\frac{\partial T}{\partial z}$  at the Hesperian and Amazonian volcanic constructs shown in Figure 14 are likely upper bounds for the corresponding globally averaged values. The results presented in Figure 14 indicate rapid declines of thermal gradient and heat flux with time in the early (Noachian) history of Mars, followed by more modest rates of decline in later epochs. Such a pattern is consistent with the predictions of thermal history models based on parametrized mantle convection [e.g., Stevenson et al., 1983; Schubert et al., 1992].

We may compare our estimates of lithospheric thermal gradient and heat flow with those of earlier workers. *Solomon and Head* [1990] concluded that substantial variations in thermal gradient and heat flux were present during the Amazonian epoch, because of the large inferred differences in  $T_e$  between Olympus Mons (and ‘‘Tharsis’’ in general) and the Tharsis Montes found by *Comer et al.* [1985]. Such variations are not consistent with the new  $T_e$  estimates

for features with Amazonian-aged surfaces given in Table 3. It is now clear that the low  $T_e$  estimates for Tharsis Montes reported by *Comer et al.* [1985] were the result of an incorrect interpretation of graben, now known to lie on the flanks of the edifices on the basis of MGS altimetry, as due to flexural stresses in the lithosphere. Instead, the extensional stress state required to form flank graben is likely caused by either edifice sliding or spreading [McGovern and Solomon, 1993] or intrusion and uplift [McGovern et al., 2001; Montesi, 2001]. Estimates of  $T_e$  from a purely flexural interpretation of Tharsis Montes flank graben will be biased to low values, such that the flexural wavelength is sufficiently low to predict a maximum extensional stress on the flank. Of the  $T_e$  estimates given by *Comer et al.* [1985] and used by *Solomon and Head* [1990], MGS observations indicate that only those for Olympus Mons and the Isidis basin are likely to be valid. The former estimate was based on the absence of load-induced graben, while the latter estimate was based on the positions of the basin-encircling graben beyond the edge of the mascon load.

There are further differences between our results and those of *Solomon and Head* [1990] and other workers. Given a wide range of inferred values for heat flux and thermal gradient for features with Amazonian-aged surfaces, and moderate-to-low inferred values for pre-Amazonian structures (such as Alba Patera, the Elysium rise, and the Isidis basin), no clear temporal trend in these quantities was found by *Comer et al.* [1985]. In contrast, we find a general trend of decreasing values of  $\frac{\partial T}{\partial z}$  and  $q$  with the surface age of a feature (Figure 14). The moderate flux inferred for the southern Hellas rim and the low heat flux inferred for Valles Marineris (Figure 14b), as well as for Isidis by *Solomon and Head* [1990], nonetheless suggest significant spatial heterogeneity in thermal gradient and heat flow prior to the Amazonian.

Our results may be compared and contrasted to those of other studies that have used MGS gravity and topography data. Our upper bounds on  $q$  at Valles Marineris are inconsistent with the lower bound of 20 mW/m $^2$  reported by *Anderson and Grimm* [1998]. Poor resolution of older gravity and topography solutions and the use of a purely spatial-domain method for estimating  $T_e$  by *Anderson and Grimm* [1998] may account for the difference. In contrast, estimates of  $\frac{\partial T}{\partial z}$  at Valles Marineris by *Schultz and Lin* [2001], obtained from forward models of deformation due to normal faulting and small measured footwall uplifts, yield an upper bound of 10 K/km, broadly consistent with our results. Our estimates of  $\frac{\partial T}{\partial z}$  at Olympus Mons and the Tharsis Montes are also generally lower than the 7–10 K/km range for central Tharsis found by *Arkani-Hamed* [2000]. The model gravity calculations of *Arkani-Hamed* [2000] did not take into account finite-amplitude effects (see Appendix C); the dense buried loads at Tharsis volcanoes inferred by *Arkani-Hamed* [2000] are likely artifacts of this choice. Such loads allow models with lower  $T_e$  to fit the observed gravity, resulting in higher heat flux estimates. Several of our  $T_e$  estimates for individual features in Tharsis, Valles Marineris, and Elysium differ significantly from estimates given by *McKenzie et al.* [2002] for the regions enclosing them. This is likely because admittance signals from these features are diluted by averaging with signals from other features contained within the broad areas used by *McKenzie et al.* [2002]. In contrast, the relatively compact localization windows used in this study

**Table 3.** Summary of Thermal Gradient and Heat Flux Estimates

Feature	Surface age <sup>1</sup>	$T_e$ , km	Thermal gradient, K/km	Heat flux, mW/m <sup>2</sup>	$L_{win}$	$l$ range for fit	Load density <sup>2</sup> $\rho_l$ , kg/m <sup>3</sup>	Bottom loading, $f$
Olympus Mons <sup>3</sup>	A	> 140	< 5	< 18	10	16–50	2900	0
Ascraeus Mons <sup>3</sup>	A	70–160	4–9	14–26	15	18–45	3050	0
Pavonis Mons <sup>3</sup>	A	80–170	4–8	14–25	15	18–35	3100	0
Arsia Mons <sup>3,4</sup>	A	20–70	6–13	15–33	15	18–30	3100–3150	0
Alba Patera <sup>3,4</sup>	A-H	40–60	6–14	15–35	10	13–35	2900	0–0.1
Elysium rise <sup>3</sup>	A-H	50–80	7–12	21–30	10	13–50	3000	0
Hebes Chasma <sup>5</sup>	A-H	> 80	< 9	< 28	15	18–45	2900	0.7
Hebes Chasma <sup>5,6,7</sup>	A-H	60–130	5–9	14–25	15	18–45	1900–2200	0
Candor Chasma <sup>5</sup>	A-H	> 160	< 4.5	< 16	15	18–45	2900	0.6
Candor Chasma <sup>5,6,7</sup>	A-H	> 120	< 5.5	< 19	15	18–45	2100	0
Capri Chasma <sup>5</sup>	A-H	> 130	< 5.5	< 19	15	18–45	2900	0.3
Capri Chasma <sup>5,6,7</sup>	A-H	> 120	< 6	< 20	15	18–45	2400	0
Solis Planum <sup>5,8</sup>	H	20–35	8.5–15	21–38	10	13–30	2900	0
Hellas south rim <sup>5,8</sup>	H-N	< 25	> 9	> 22	15	18–45	2900	0
Hellas south rim <sup>5,9</sup>	H-N	60–200	3.5–11	13–30	15	18–45	2900	0.3–0.6
Hellas west rim <sup>5,8</sup>	H-N	< 15	> 13	> 32	15	18–45	2900	0
Hellas basin <sup>5,8</sup>	N	< 10	> 19	> 47	5	8–55	2900	0
Noachis Terra <sup>5,8</sup>	N	< 13	> 21	> 52	15	18–45	2650	0
Northeastern Terra Cimmeria <sup>5,8</sup>	N	< 12	> 18	> 45	15	18–45	2900	0
Northeastern Arabia Terra <sup>5,8</sup>	N	< 15	> 19	> 47	15	18–45	2400	0

<sup>1</sup> The letters A, H, and N refer to Amazonian, Hesperian, and Noachian epochs, respectively.

<sup>2</sup> Load density varied in increments of 50 kg/m<sup>3</sup> unless otherwise noted.

<sup>3</sup> Crustal density  $\rho_c$  taken to be equal to nominal value (2900 kg/m<sup>3</sup>, Table 1).

<sup>4</sup> Parameter ranges reflect the possibility that lithospheric ductile strength may be limited by that of either diabase or olivine.

<sup>5</sup> Crustal density  $\rho_c$  taken to be equal to load density  $\rho_l$ .

<sup>6</sup> Load density varied in increments of 100 kg/m<sup>3</sup>.

<sup>7</sup> Alternate solution with low surface density,  $f = 0$ .

<sup>8</sup> Ductile strength taken to be that of diabase.

<sup>9</sup> Alternate solution with bottom loading.

enable us to isolate the admittance signatures of individual features (volcanoes, chasm segments, etc.) from those of their surroundings, allowing us to gather both more refined and more numerous estimates of  $T_e$ . Nonetheless, our results confirm earlier suggestions, based on admittance analysis of MGS gravity and topography data for limited numbers of regions [Zuber et al, 2000; McKenzie et al., 2002], that the lithosphere of Mars has thickened and the planet has cooled with time.

Estimates of  $T_e$  for the ancient southern uplands have further implications for the early (Noachian) thermal and magnetic history of Mars. The topography of the cratered uplands and the Hellas basin was Airy compensated, or nearly so, at the time of formation (Figures 11, 13). However, such topography will tend to decay with time due to ductile flow in the lower crust [e.g., Zuber et al., 2000, Nimmo and Stevenson, 2001], a process facilitated by high temperatures. The fact that this topography was preserved to the present implies that after the topography formed the lithosphere cooled sufficiently rapidly to arrest lower crustal flow (and remained cool thereafter). A relatively rapid decline in heat flow in the early history of Mars is consistent with predictions of thermal history models (with parameterized mantle convection) based on a decline in radiogenic heating with time [e.g., Stevenson et al., 1983; Schubert et al., 1992]. The mechanical lithosphere thickness  $T_m$  defines the depth to an isotherm in the lithosphere near 550–600 °C, depending on strain rate [McNutt, 1984]. This isotherm is close to the Curie temperature for common magnetic minerals. It has been argued that magnetic anomalies observed in Terrae Cimmeria and Sirenum suggest a depth extent of magnetization of several tens of kilometers [Connerney et al, 1999; Nimmo, 2000], although this figure depends on the assumed

value for specific magnetization. Such a depth extent significantly exceeds estimates for  $T_e$  at Terrae Cimmeria and Sirenum at the time the present gravity/topography relationship was established. Either magnetization postdated that time by an amount sufficient for significant cooling and thickening of the lithosphere, or values of specific magnetization higher than typically assumed must be postulated.

## 5. Conclusions

We have analyzed gravity and topography data from the MGS mission, using a spatio-spectral localization method, a new model of elastic spherical shell flexure subject to surface and subsurface loading, and a model gravity calculation that takes into account the significant effects of finite-amplitude relief. Localized estimates of gravity-shape admittance and correlation spectra were obtained for a variety of regions on Mars. Such estimates were compared with predictions from flexure models to obtain estimates of the elastic lithosphere thickness  $T_e$  (at the time of loading) for terrains of diverse age and provenance.

Admittances are generally high in regions dominated by volcanic edifices with Amazonian-aged surfaces, including central Tharsis, Olympus Mons, and the domal rises Alba Patera and Elysium. In such regions the signal of large surface loads (volcanic edifices) dominates, obscuring the signatures of earlier loading events. At the Tharsis Montes, admittance spectra indicate high  $T_e$  (somewhat lower at Arsia Mons) and load densities slightly higher (3000–3150 kg/m<sup>3</sup>) than the nominal value (2900 kg/m<sup>3</sup>; Table 1). Neither further increases in load density nor dense subsurface loads [e.g., Arkani-Hamed, 2000], however, are required to fit the

gravity and shape data at the Tharsis Montes. Intermediate values of  $T_e$  are obtained for the domal rises Alba Patera and Elysium, consistent with an intrusion-based scenario for building domal rises [McGovern *et al.*, 2001]. The  $T_e$  estimates for Arsia Mons overlap the range for domal rises, suggesting the possibility of a similar evolutionary path for that edifice or its precursor. Admittance and correlation spectra at Valles Marineris indicate relatively uncompensated topography and are consistent with either emplacement of substantial subsurface loads or troughs cut into low-density crust. Large negative to positive shifts in admittance and correlation spectra for the large impact basins indicate the presence of subsurface loads (mascons). The presence of significant positive and negative gravity anomalies with no corresponding topographic signature in the northern lowlands also implies subsurface loads. The southern highlands of Mars, including regions with large magnetization anomalies, are characterized by low admittance values (but high correlations), yielding low estimates of  $T_e$  and load densities. Given the similarity between the temperature defining the base of the mechanical lithosphere and the Curie temperature for common magnetic minerals, our  $T_e$  estimates (< 30 km) constrain either the timing of magnetization to be later than that at which gravity/topography relations were established or the magnitude of specific magnetization to be greater than often assumed.

By converting estimates of  $T_e$  to estimates lithospheric thermal gradient  $\frac{\partial T}{\partial z}$  and heat flux  $q$ , we show that  $\frac{\partial T}{\partial z}$  and  $q$  are generally greater for regions with older surfaces. The long-term preservation of nearly Airy-compensated terrain of the Hellas Basin and portions of the southern highlands of Mars requires that early cooling of the lower crust was sufficiently rapid to “freeze in” lateral heterogeneity in crustal thickness against ductile flow of the lower crust. These findings are consistent with the secular cooling of the Martian interior and with a rate of cooling that was particularly high in the Noachian.

## Appendix A: Loading of a Thin Elastic Shell

To solve for deflections of a thin elastic spherical shell, we adopt a modified version of the formulation of *Turcotte et al.* [1981], which is based on the derivation of *Kraus* [1967]. For a shell with radius  $R$  and thickness  $T_e$ , the deflection  $w$  (here considered positive upwards) is governed by

$$D\nabla^6 w + 4D\nabla^4 w + ET_e R^2 \nabla^2 w + 2ET_e R^2 w = -R^4 (\nabla^2 + 1 - \nu)p, \quad (\text{A1})$$

where the flexural rigidity  $D = ET_e^3/12(1-\nu^2)$ ,  $E$  is Young’s modulus,  $\nu$  is Poisson’s ratio, and  $p$  is the loading pressure on the shell (also positive upwards). The pressure  $p_t$  induced by a surface (or “top”) load of height  $h$  is given by

$$p_t = -g[\rho_l h + (\rho_m - \rho_l)w], \quad (\text{A2})$$

where  $g$  is the acceleration of gravity,  $\rho_l$  the load density, and  $\rho_m$  the mantle density. The formulation of *Turcotte et al.* [1981] has been modified to account for a load density  $\rho_l$  that differs from the crustal density  $\rho_c$ . Furthermore, we account for self-gravitation differently than did *Turcotte et al.* [1981], through our explicit assumption (Equation 1) that  $h$  is equipotentially referenced (compare Equation A2 with Equation 3 of *Turcotte et al.* [1981]).

In Equation A2 it is assumed that the mantle behaves as a fluid on loading timescales, providing a restoring force

proportional to  $w$ . The  $\rho_l w$  term represents infill of the flexural depression with material of that density. We expand  $h$  (and  $w$ ) in terms of spherical harmonics

$$h(\theta, \phi) = R \sum_l \sum_{m=0}^l \sum_{i=1}^2 h_{ilm} Y_{ilm}(\theta, \phi) \quad (\text{A3})$$

where  $Y_{ilm}$  is the normalized spherical harmonic function of degree  $l$  and order  $m$ ,  $\theta$  is colatitude, and  $\phi$  is longitude. The equation for  $w$  is then

$$w_{ilm} = h_{ilm} \alpha_l^t. \quad (\text{A4})$$

The transfer function  $\alpha_l^t$  is given by

$$\alpha_l^t = - \left( \frac{\rho_l}{\rho_m - \rho_l} \right) \left\{ \frac{l(l+1) - (1-\nu)}{\sigma f_1(l) + \tau f_2(l) + l(l+1) - (1-\nu)} \right\}, \quad (\text{A5})$$

where  $f_1(l) = l^3(l+1)^3 - 4l^2(l+1)^2$   $f_2(l) = l(l+1) - 2$ , and

$$\tau \equiv \frac{ET_e}{R^2 g(\rho_m - \rho_l)}, \quad (\text{A6})$$

and

$$\sigma \equiv \frac{D}{R^4 g(\rho_m - \rho_l)} = \frac{\tau}{12(1-\nu^2)} \left( \frac{T_e}{R} \right)^2. \quad (\text{A7})$$

For subsurface (or “bottom”) loading, we assume that the induced surface height  $h_b$  corresponds to the deflection of the lithosphere resulting from a subsurface load with thickness  $w_b$  and density anomaly  $\rho_b$ . We start with the equation for spherical shell flexure [*Turcotte*, 1981]:

$$D\nabla^6 h_b + 4D\nabla^4 h_b + ET_e R^2 \nabla^2 h_b + 2ET_e R^2 h_b = -R^4 (\nabla^2 + 1 - \nu)p_b, \quad (\text{A8})$$

where the load pressure  $p_b$  is given by

$$p_b = -g[\rho_b w_b + \rho_m h_b]. \quad (\text{A9})$$

Solving for  $w_b$  we obtain

$$w_b = h_b \alpha_l^b, \quad (\text{A10})$$

where

$$\alpha_l^b = - \left( \frac{\rho_m}{\rho_b} \right) \left\{ \frac{\sigma' f_1(l) + \tau' f_2(l) + l(l+1) - (1-\nu)}{l(l+1) - (1-\nu)} \right\}, \quad (\text{A11})$$

$$\tau' \equiv \frac{ET_e}{R^2 g \rho_m}, \quad (\text{A12})$$

and

$$\sigma' \equiv \frac{D}{R^4 g \rho_m} = \frac{\tau'}{12(1-\nu^2)} \left( \frac{T_e}{R} \right)^2. \quad (\text{A13})$$

## Appendix B: Combined Surface and Subsurface Loading

We follow the derivation of combined flexural loading presented in Equations 14–20 of *Forsyth* [1985]. We drop degree and order subscripts, with the implicit understanding that the following derivation applies to individual harmonic coefficients. The surface height  $h$  (depth  $z = 0$ ) is the sum of relief produced by both surface and subsurface loading:

$$h = h_t + h_b, \quad (\text{B1})$$

and subsurface deflections are handled similarly:

$$w = w_t + w_b. \quad (\text{B2})$$

The expression for the initial surface load  $h_i$  accounts for the material that fills the underlying load-induced deflection ( $w_t$ ):

$$h_i = h_t - w_t. \quad (\text{B3})$$

The bottom load is modeled in terms of the thickness  $w_b$  of a layer of material with density anomaly  $\rho_b$  (in the sense of *McNutt* [1983]), rather than as relief on a density contrast interface (as in *Forsyth* [1985]). This distinction is important, both for determining the amplitude of the initial subsurface load  $w_i$ :

$$w_i = w_b, \quad (\text{B4})$$

and for the gravity calculation (see below). If the subsurface load consists of relief on a density interface, equation B4 would have an extra  $-h_b$  term [*Forsyth*, 1985].

We seek to solve for the four quantities  $h_t$ ,  $h_b$ ,  $w_t$ , and  $w_b$ , given the observed topography  $h$  and the ratio of subsurface to surface loading  $f$ :

$$f = -\frac{w_i \rho_b}{h_i \rho_l} = -\frac{w_b \rho_b}{h_i \rho_l}, \quad (\text{B5})$$

and the relations

$$w_t = \alpha^t h_t \quad (\text{B6})$$

and

$$w_b = \alpha^b h_b. \quad (\text{B7})$$

The minus sign in equation B5 is required because positive  $w_b$  leads to negative  $h_b$ , whereas positive  $h_t$  leads to positive  $h$ .

First, we solve for  $h_i$  and  $w_i$ :

$$h_i = h_t(1 - \alpha^t), \quad (\text{B8})$$

$$w_i = w_b = \alpha^b h_b. \quad (\text{B9})$$

Then

$$h = h_t + h_b = \frac{h_i}{(1 - \alpha^t)} + \frac{w_b}{\alpha^b}. \quad (\text{B10})$$

Substituting for  $h_i$ ,

$$h = w_b \left[ -\frac{\rho_b}{\rho_l} \frac{1}{f(1 - \alpha^t)} + \frac{1}{\alpha^b} \right] = w_b \Phi. \quad (\text{B11})$$

Then

$$w_b = \frac{h}{\Phi}, \quad (\text{B12})$$

and we obtain  $h_b$  from Equation B7,  $h_t$  from Equation B1, and  $w_t$  from Equation B6. For  $f = 0$ ,  $\Phi$  is infinite, and by Equation B1  $w_b = 0$ .

Given the relief on density interfaces from these equations, we can calculate gravitational potential coefficients for any given model. The relief, density contrast, and reference depth corresponding to each interface are given in Table 2. The uppermost interface is simply the observed shape. The upper and lower surfaces of the crust have relief induced by both the top ( $w_t$ ) and bottom ( $h_b$ ) loads. The original bottom load of magnitude  $w_b$  is assumed to be emplaced at the reference depth  $z_b$ ; however, this original configuration is displaced in the same manner as the crustal surfaces (hence the  $h_b + w_t$  term). Two expansions are required to describe the gravity contribution of the bottom load: one with  $w_b$  plus the subsurface deformation with density contrast  $\rho_b$ , and another with only the subsurface deformation and  $-\rho_b$ , to account for the difference between ambient and anomalous density.

## Appendix C: Necessity of the Finite-amplitude Correction and Its Implementation

The method used to model gravity perturbations resulting from relief on density interfaces can strongly influence interpretations of MGS-derived gravity fields and admittances. Here we demonstrate the requirement that finite-amplitude effects be included in the model gravity calculations and illuminate several potential pitfalls in the modeling process.

The standard modeling approach in harmonic gravity/topography studies is to apply the observed topography as a load on the lithosphere, determine the resulting lithosphere deflection, and calculate the gravity field resulting from density interfaces at the surface (topography) and crust-mantle boundary (deflection). The latter calculations are commonly performed under an approximation treating the interfaces as mass sheets with magnitudes equal to the product of relief and an appropriate density contrast. Under the mass-sheet approximation, gravity/topography admittance spectra approach a constant value with increasing  $T_e$  (the “rigid limit”). At Olympus Mons, for instance, the nominal model yields a rigid-limit admittance that falls far

**Figure C1.** Gravity/topography and gravity/shape admittances for Olympus Mons, localized with a 2000-km-diameter window ( $L_{win} = 10$ ). (a) Comparison of admittances for MGS topography and gravity data (solid line with error bars) with admittances for MGS topography data and modeled gravity from flexure models with  $T_e = 200$  km: mass-sheet gravity calculation and nominal density model (dashed line), mass-sheet gravity calculation and  $\rho_l = 3300$  kg/m<sup>3</sup> (thin solid line with dots), and gravity calculation with the finite-amplitude topography correction and the nominal density model (circles). (b) Comparison of admittances for MGS shape and gravity data (solid line with error bars) with admittances for MGS shape data and gravity from finite-amplitude topography for flexure models with  $T_e = 200$  km (circles).

short of the observed values (the dashed line in Figure C1a). In order to match the observations, models with buried excess loads correlated with topography [Arkani-Hamed *et al.*, 2000] or surface densities in excess of  $3300 \text{ kg/m}^3$  [McGovern *et al.*, 2000] are required; the former would induce horizontal compressive edifice stresses [McGovern and Solomon 1993, 1998] inconsistent with the presence of areally large volcanic flows on the surface of the edifice and draping over the flanks and basal scarp, and the latter works only over a limited wavenumber band (thin solid line in Figure C1a).

However, with the calculation of gravity from finite-amplitude topography [Wieczorek and Phillips, 1998], the resulting model admittance curves more closely match the observed curve in both magnitude and shape. The upturn at high  $l$  (circles, Figure C1a) is caused by the increased attraction of the short-wavelength near-summit topography atop the longer-wavelength high of the Olympus Mons edifice. In order to account fully for this coupling of short and long wavelengths, the radii from the center of mass, or shape, must be used instead of the equipotentially-referenced topography. In other words, the relief used for the gravity calculation must be referenced to a sphere rather than to an equipotential. In practice, we still use the equipotentially-referenced topography as the surface load, but we add the areoid height to the deflections to determine the radial locations of density interfaces in the model gravity calculation. In this way we avoid modeling the rotational flattening of the planet as a surface load. Thus, harmonic expansions of both topography and shape are required to carry out the modeling correctly. Use of only one of these expansions will produce incorrect results. When properly calculated, the nominal model admittance (circles, Figure C1b) and observed admittance curves at Olympus Mons match very closely. This correction will affect admittances for short-wavelength topography atop longer-wavelength highs (e.g., the Tharsis Montes and rise and the cratered southern uplands) and lows (e.g., the northern lowlands and large basins). The planetary shape component of the correction will be greatest near the equator and at the poles, due to rotational flattening.

**Acknowledgments.** We thank Francis Nimmo and Norman Sleep for constructive reviews, and Mary Chapman, Walter Kiefer, Richard Schultz, and Kenneth Tanaka for helpful discussions. This research was supported by the National Aeronautics and Space Administration under grants NAG 5-4436, NAG 5-4077, and NAG 5-10165 (to the Carnegie Institution of Washington), and NASW-4574 (to the Lunar and Planetary Institute, operated by the Universities Space Research Association). This paper is Lunar and Planetary Institute Contribution 1121.

## References

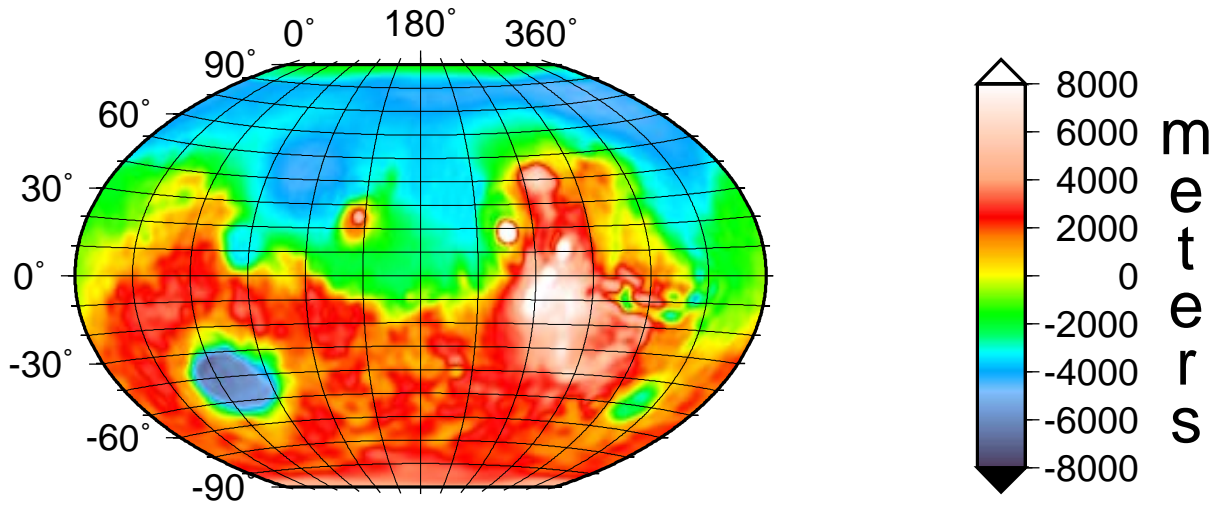
- Acuña, M. H., *et al.*, Global distribution of crustal magnetization discovered by the Mars Global Surveyor MAG/ER experiment, *Science*, *284*, 790–793, 1999.
- Albert, R. A., and R. J. Phillips, Paleoflexure, *Geophys. Res. Lett.*, *27*, 2385–2388, 2000.
- Anderson, E. M., *The Dynamics of Faulting and Dyke Formation with Applications to Britain*, Oliver and Boyd, Edinburgh, 2nd ed., 206 pp., 1951.
- Anderson, F. S., and W. B. Banerdt, Preliminary admittance estimates for the Valles Marineris, Mars, *Lunar Planet. Sci.*, *31*, abstract 2090, Lunar and Planetary Institute, Houston (CD-ROM), 2000.
- Anderson, R. C., J. M. Dohm, M. P. Golombek, A. F. C. Halde-mann, B. J. Franklin, K. L. Tanaka, J. Lias, and B. Peer, Primary centers and secondary concentrations of tectonic activity through time in the western hemisphere of Mars, *J. Geophys. Res.*, *106*, 20,563–20,585, 2001.
- Anderson, S., and R. E. Grimm, Rift processes at the Valles Marineris, Mars: Constraints from gravity on necking and rate-dependent strength evolution, *J. Geophys. Res.*, *103*, 11,113–11,124, 1998.
- Arkani-Hamed, J., Strength of Martian lithosphere beneath large volcanoes *J. Geophys. Res.*, *105*, 26,713–26,732, 2000.
- Banerdt, W. B., Support of long-wavelength loads on Venus and implications for internal structure, *J. Geophys. Res.*, *91*, 403–419, 1986.
- Banerdt, W. B., and A. Vidal, Surface drainage on Mars, *Lunar Planet. Sci.*, *32*, abstract 1488, Lunar and Planetary Institute, Houston (CD-ROM), 2001.
- Banerdt, W. B., R. J. Phillips, N. H. Sleep, and R. S. Saunders, Thick shell tectonics on one-plate planets: Applications to Mars, *J. Geophys. Res.*, *87*, 9723–9733, 1982.
- Banerdt, W. B., M. P. Golombek and K. L. Tanaka, Stress and tectonics on Mars, in *Mars*, edited by H. H. Kieffer, B. M. Jakosky, C. W. Snyder, and M. S. Matthews, pp. 249–297, Univ. of Ariz. Press, Tucson, 1992.
- Buck, W. R., Modes of continental lithospheric extension, *J. Geophys. Res.*, *96*, 20,161–20,178, 1991.
- Byerlee, J. D., Friction of rocks, *Pure Appl. Geophys.*, *116*, 615–626, 1978.
- Caristan, Y., The transition from high temperature creep to fracture in Maryland diabase, *J. Geophys. Res.*, *87*, 6781–6790, 1982.
- Carr, M. H., Volcanism on Mars, *J. Geophys. Res.*, *78*, 4049–4062, 1973.
- Comer, R. P., S. C. Solomon, and J. W. Head, Mars: Thickness of the lithosphere from the tectonic response to volcanic loads, *Rev. Geophys.*, *23*, 61–92, 1985.
- Connerney, J. E. P., *et al.*, Magnetic lineations in the ancient crust of Mars, *Science*, *284*, 794–798, 1999.
- Crown, D. A., and R. Greeley, Volcanic geology of Hadriaca Patera and the eastern Hellas region of Mars, *J. Geophys. Res.*, *98*, 3431–3451, 1993.
- Crumpler, L. S., and J. C. Aubele, Structural evolution of Arsia Mons, Pavonis Mons, and Ascresus Mons: Tharsis region of Mars, *Icarus*, *34*, 496–511, 1978.
- Dohm, J. M., and K. L. Tanaka, Geology of the Thaumasia region, Mars: Plateau development, valley origins, and magmatic evolution, *Planet. Space Sci.*, *47*, 411–431, 1999.
- Dohm, J. M., J. C. Ferris, V. R. Baker, R. C. Anderson, T. M. Hare, R. G. Strom, N. G. Barlow, K. L. Tanaka, J. E. Klemaszewski, and D. H. Scott, Ancient drainage basin of the Tharsis region, Mars: Potential source for outflow channel systems and putative oceans or paleolakes *J. Geophys. Res.*, *106*, 32,943–32,957, 2001.
- Ernst, R. E., E. B. Grosfils and D. Mège, Giant dike swarms: Earth, Venus And Mars, *Annu. Rev. Earth Planet. Sci.*, *29*, 489–534, 2001.
- Evans, B. and C. Goetze, The temperature variation of hardness of olivine and its implication for polycrystalline yield stress, *J. Geophys. Res.*, *84*, 5505–5524, 1979.
- Folkner, W. M., C. F. Yoder, D. N. Yuan, E. M. Standish, and R. A. Preston, Interior structure and seasonal mass redistribution of Mars from radio tracking of Mars Pathfinder, *Science*, *278*, 1749–1752, 1997.
- Forsyth, D. W., Subsurface loading and estimates of the flexural rigidity of continental lithosphere, *J. Geophys. Res.*, *90*, 12,623–13,632, 1985.
- Frey, H. V., K. M. Shockey, E. L. Frey, J. H. Roark, and S. E. H. Sakimoto, A very large population of likely buried impact basins in the northern lowlands of Mars revealed by MOLA data, *Lunar Planet. Sci.*, *32*, abstract 1680, Lunar and Planetary Institute, Houston (CD-ROM), 2001.
- Goetze, C., The mechanisms of creep in olivine, *Philos. Trans. R. Soc. London, Ser. A*, *288*, 99–119, 1978.
- Greeley, R., and J. E. Guest, Geologic map of the eastern equatorial region of Mars, *U. S. Geol. Surv. Misc. Invest. Ser. Map I-1802-B*, scale 1:15,000,000, 1987.
- Hall, J. L., S. C. Solomon, and J. W. Head, Elysium region, Mars: Tests of lithospheric loading models for the formation of tectonic features, *J. Geophys. Res.*, *91*, 11,377–11,392, 1986.



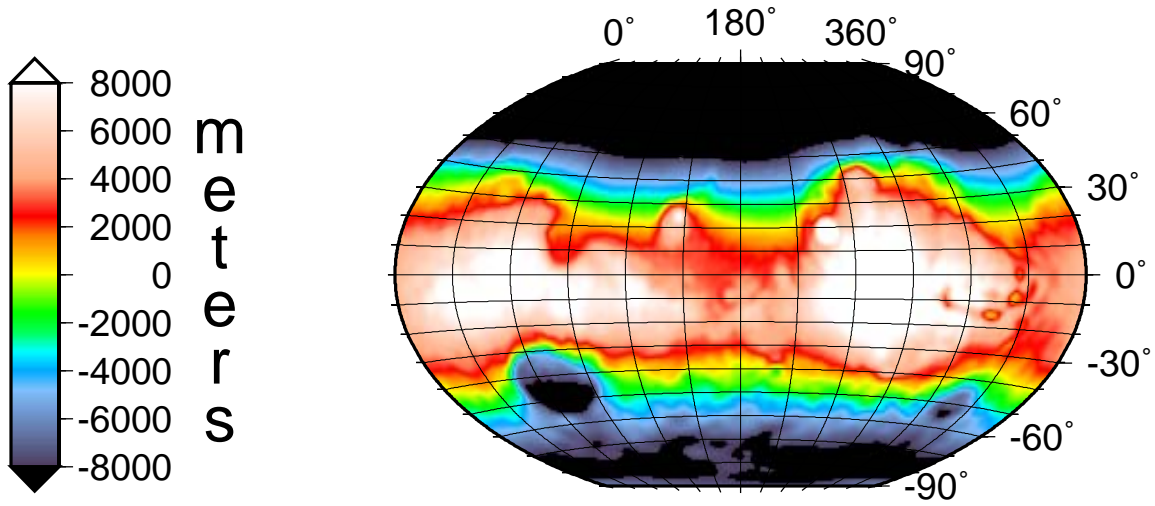
- Head, J. W., III, M. A. Kreslavsky, and S. Pratt, Northern lowlands of Mars: Evidence for widespread volcanic flooding and tectonic deformation in the Hesperian period, *J. Geophys. Res.*, *107* 10.1029/2000LE001445, 2002.
- Hynek, B. M., and R. J. Phillips, Evidence for extensive denudation of the Martian highlands, *Geology*, *29*, 407–410, 2001.
- Janle, P., and D. Jannsen, Isostatic gravity and elastic bending models of Olympus Mons, Mars, *Ann. Geophys.*, *4B*, 537–546, 1986.
- Janle, P., and E. Erkul, Gravity studies of the Tharsis area of Mars, *Earth Moon Planets*, *53*, 217–232, 1991.
- Lemoine, F. G., D. E. Smith, D. D. Rowlands, M. T. Zuber, G. A. Neumann, D. S. Chinn, and D. E. Pavlis, An improved solution of the gravity field of Mars (GMM-2B) from Mars Global Surveyor, *J. Geophys. Res.*, *106*, 23,359–23,376, 2001.
- McEwen, A. S., M. C. Malin, M. H. Carr, and W. K. Hartmann, Voluminous volcanism on early Mars revealed in Valles Marineris, *Nature*, *397*, 584–586, 1999.
- McGill, G. E., Buried topography of Utopia, Mars: Persistence of a giant impact depression, *J. Geophys. Res.*, *94*, 2753–2759, 1989.
- McGovern, P. J., and S. C. Solomon, State of stress, faulting, and eruption characteristics of large volcanoes on Mars, *J. Geophys. Res.*, *98*, 23,553–23,579, 1993.
- McGovern, P. J., and S. C. Solomon, Filling of flexural moats around large volcanoes on Venus: Implications for volcano structure and global magmatic flux, *J. Geophys. Res.*, *102*, 16,303–16,318, 1997.
- McGovern, P. J., and S. C. Solomon, Growth of large volcanoes on Venus: Mechanical models and implications for structural evolution, *J. Geophys. Res.*, *103*, 11,071–11,101, 1998.
- McGovern, P. J., S. C. Solomon, D. E. Smith, M. T. Zuber, G. A. Neumann, and J. W. Head, Localized gravity/topography admittances on Mars, *Lunar Planet. Sci.*, *31*, abstract 1792, Lunar and Planetary Institute, Houston (CD-ROM), 2000.
- McGovern, P. J., S. C. Solomon, J. W. Head, D. E. Smith, M. T. Zuber, and G. A. Neumann, Extension and uplift at Alba Patera, Mars: Insights from MOLA observations and loading models, *J. Geophys. Res.*, *106*, 23,769–23,809, 2001.
- McKenzie, D., and F. Nimmo, The generation of martian floods by the melting of ground ice above dikes, *Nature*, *397*, 231–233, 1999.
- McKenzie, D., D. N. Barnett, and D.-H. Yuan, The relationship between Martian gravity and topography, *Earth Planet. Sci. Lett.*, *195*, 1–16, 2002.
- McNutt, M. K., Influence of plate subduction on isostatic compensation in northern California, *Tectonics*, *2*, 399–415, 1983.
- McNutt, M. K., Lithospheric flexure and thermal anomalies, *J. Geophys. Res.*, *89*, 11,180–11,194, 1984.
- Mège, D., and P. Masson, Amounts of crustal stretching in Valles Marineris, Mars, *Planet. Space Sci.*, *44*, 749–782, 1996a.
- Mège, D., and P. Masson, A plume tectonics model for the Tharsis province, Mars, *Planet. Space Sci.*, *44*, 1499–1546, 1996b.
- Montési, L. G. J., Concentric dikes on the flanks of Pavonis Mons: Implications for the evolution of Martian shield volcanoes and mantle plumes, in *Identifying and Locating Mantle Plumes Through Geologic Time*, edited by R. E. Ernst and K. L. Buchan, *Geol. Soc. Am. Spec. Paper 352*, 165–181, 2001.
- Neukum, G., and K. Hiller, Martian ages, *J. Geophys. Res.*, *86*, 3097–3121, 1981.
- Nimmo, F., Dike intrusion as a possible cause of linear Martian magnetic anomalies, *Geology*, *28*, 391–394, 2000.
- Nimmo, F., and D. Stevenson, Estimates of Martian crustal thickness from viscous relaxation of topography, *J. Geophys. Res.*, *106*, 5085–5098, 2001.
- Parker, R. L., The rapid calculation of potential anomalies, *Geophys. J. Roy. Astron. Soc.*, *31*, 447–455, 1972.
- Petit, C., and C. Ebinger, Flexure and mechanical behavior of cratonic lithosphere: Gravity models of the East African and Baikal Rifts, *J. Geophys. Res.*, *105*, 19,151–19,162, 2000.
- Phillips, R. J., M. T. Zuber, B. M. Hynek, and K. B. Portle, Mars: Are negative linear gravity anomalies buried fluvial channels?, *Lunar Planet. Sci.*, *32*, abstract 1176, Lunar and Planetary Institute, Houston (CD-ROM), 2001.
- Plescia, J. B., and R. S. Saunders, The chronology of the martian volcanoes, *Proc. Lunar Planet. Sci.*, *10*, 2841–2859, Lunar and Planetary Institute, Houston, Tex., 1979.
- Pollard, D. D., Elementary fracture mechanics applied to the structural interpretation of dykes, in *Mafic Dyke Swarms*, edited by H. C. Halls and W. F. Fahrig, *Geol. Assoc. Canada Spec. Paper 34*, 5–24, 1987.
- Schubert, G., S. C. Solomon, D. L. Turcotte, M. J. Drake, and N. H. Sleep, Origin and thermal evolution of Mars, in *Mars*, edited by H. H. Kieffer, B. M. Jakosky, C. W. Snyder, and M. S. Matthews, pp. 147–183, Univ. of Ariz. Press, Tucson, 1992.
- Schultz, R. A., Brittle strength of basaltic rock masses with applications to Venus, *J. Geophys. Res.*, *98*, 10,883–10,895, 1993.
- Schultz, R. A., and J. Lin, Three-dimensional normal faulting models of the Valles Marineris, Mars, and geodynamic implications, *J. Geophys. Res.*, *106*, 16,549–16,566, 2001.
- Schultz, R. A., and M. T. Zuber, Observations, models, and mechanisms of failure of surface rocks surrounding planetary surface loads, *J. Geophys. Res.*, *99*, 14,691–14,702, 1994.
- Scott, D. H., and K. L. Tanaka, Geologic map of the western equatorial region of Mars, *U. S. Geol. Surv. Misc. Invest. Ser. Map I-1802-A*, scale 1:15,000,000, 1986.
- Scott, E. D., and L. Wilson, Evidence for a sill emplacement event on the upper flanks of the Ascaeus Mons shield volcano, Mars, *J. Geophys. Res.*, *104*, 27,079–27,089, 1999.
- Simons, M., S. C. Solomon, and B. H. Hager, Localization of gravity and topography: Constraints on the tectonics and mantle dynamics of Venus, *Geophys. J. Int.*, *131*, 24–44, 1997.
- Sleep, N. H., and R. J. Phillips, Gravity and lithospheric stress on the terrestrial planets with reference to the Tharsis region of Mars, *J. Geophys. Res.*, *90*, 4469–4489, 1985.
- Smith, D. E., *et al.*, The global topography of Mars and implications for surface evolution, *Science*, *284*, 1495–1503, 1999a.
- Smith, D. E., *et al.*, The gravity field of Mars: Results from Mars Global Surveyor, *Science*, *286*, 94–97, 1999b.
- Smith, D. E., *et al.*, Mars Orbiter Laser Altimeter: Experiment summary after the first year of global mapping of Mars, *J. Geophys. Res.*, *106*, 23,689–23,722, 2001.
- Solomon, S. C., and J. W. Head, Heterogeneities in the thickness of the elastic lithosphere of Mars: Constraints on heat flow and internal dynamics, *J. Geophys. Res.*, *95*, 11,073–11,083, 1990.
- Stevenson, D. J., T. Spohn, and G. Schubert, Magnetism and thermal evolution of the terrestrial planets, *Icarus*, *54*, 466–489, 1983.
- Tanaka, K. L., Tectonic history of the Alba Patera-Ceraunius Fossae region of Mars, *Proc. Lunar Planet. Sci.*, *20*, 515–523, Lunar and Planetary Institute, Houston, Tex., 1990.
- Tanaka, K. L., and P. A. Davis, Tectonic history of the Syria Planum province of Mars, *J. Geophys. Res.*, *93*, 14,893–14,917, 1988.
- Thurber, C. H., and M. N. Toksöz, Martian lithospheric thickness from elastic flexure theory, *Geophys. Res. Lett.*, *5*, 977–980, 1978.
- Turcotte, D. L., R. J. Willemann, W. F. Haxby, and J. Norberry, Role of membrane stresses in support of planetary topography, *J. Geophys. Res.*, *86*, 3951–3959, 1981.
- Turcotte, D. L., R. Shcherbakov, B. D. Malamud, and A. B. Kucinskis, Is the Martian crust also the Martian elastic lithosphere, *J. Geophys. Res.*, in press, 2002.
- Turtle, E. P., and H. J. Melosh, Stress and flexural modeling of the Martian lithospheric response to Alba Patera, *Icarus*, *126*, 197–211, 1997.
- Webb, B. W., J. W. Head, B. E. Kortz, and S. Pratt, Syria Planum, Mars: A major volcanic construct in the early history of Tharsis, *Lunar Planet. Sci.*, *32*, abstract 1145, Lunar and Planetary Institute, Houston (CD-ROM), 2001.
- Wessel, P., and W. H. F. Smith, Free software helps map and display data, *Eos Trans. AGU*, *72*, 441, 1991.
- Wieczorek, M. A., and R. J. Phillips, Potential anomalies on a sphere: Applications to the thickness of the lunar crust, *J. Geophys. Res.*, *103*, 1715–1724, 1998.
- Wieczorek, M. A., and R. J. Phillips, Lunar multiring basins and the cratering process, *Icarus*, *139*, 246–259, 1999.
- Wilson, L., and J. W. Head., Tharsis-radial graben systems as surface manifestation of plume-related dike intrusion complexes: Models and implications, *Lunar Planet. Sci.*, *31*, abstract 1371, Lunar and Planetary Institute, Houston, Tex. (CD-ROM), 2000.

- Zhong, S. and M. T. Zuber, Long wavelength topographic relaxation for self-gravitating planets and implications for the time-dependent compensation of surface topography, *J. Geophys. Res.*, *105*, 4153–4164, 2000.
- Zuber, M.T., The crust and mantle of Mars, *Nature*, *412*, 220–227, 2001.
- Zuber, M. T., *et al.*, Internal structure and early thermal evolution of Mars from Mars Global Surveyor topography and gravity, *Science*, *287*, 1788–1793, 2000.
- 
- O. Aharonson, G. A. Neumann, M. A. Wieczorek, and M. T. Zuber, Department of Earth, Atmospheric, and Planetary Sciences, Massachusetts Institute of Technology, Cambridge, MA 02139. (e-mail: zuber@mit.edu)
- J. W. Head, Department of Geological Sciences, Brown University, Providence, RI 02912. (e-mail: James\_Head.III@brown.edu)
- P. J. McGovern, Lunar and Planetary Institute, 3600 Bay Area Blvd., Houston, TX 77058. (e-mail: mcgovern@lpi.usra.edu)
- R. J. Phillips, Department of Earth and Planetary Sciences, Washington University, Box 1169, One Brookings Drive, St. Louis, MO 63130. (e-mail: phillips@wustite.wustl.edu)
- M. Simons, Seismological Laboratory, Division of Geological and Planetary Sciences, 252-21 California Institute of Technology, Pasadena, CA 91125. (e-mail: simons@caltech.edu)
- D. E. Smith, NASA Goddard Flight Center, Greenbelt, MD 20771. (e-mail: dsmith@tharsis.gsfc.nasa.gov)
- S. C. Solomon, Department of Terrestrial Magnetism, Carnegie Institution of Washington, 5241 Broad Branch Road, N.W., Washington, DC 20015. (e-mail: scs@dtm.ciw.edu)

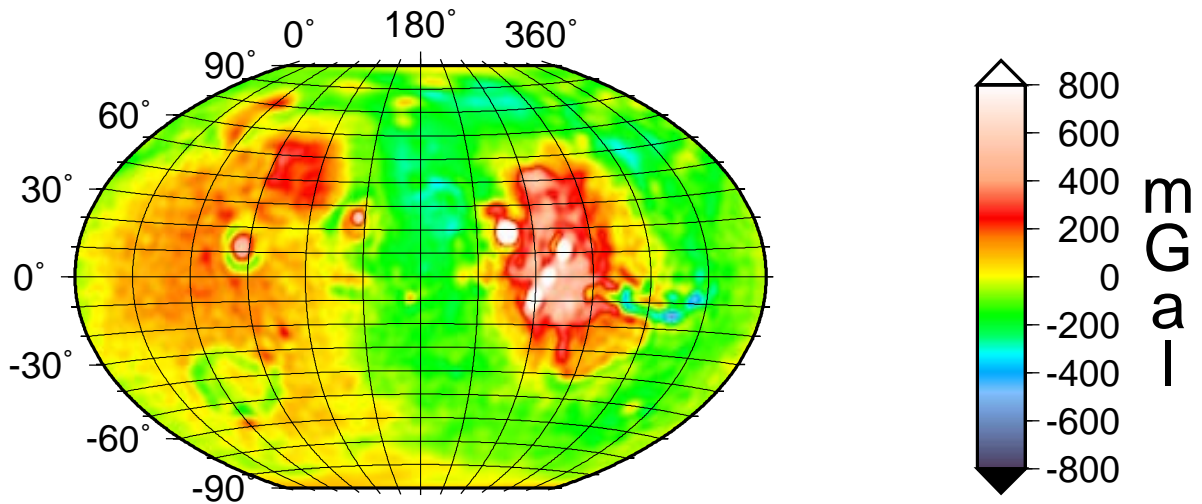
(Received \_\_\_\_\_.)



**(a) Topography: degrees 1 to 60**

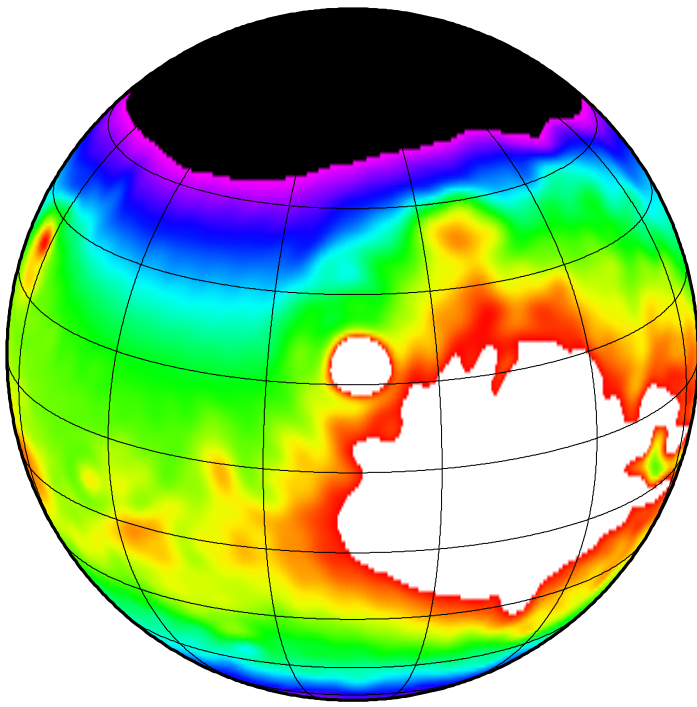


**(b) Shape: degrees 1 to 60**

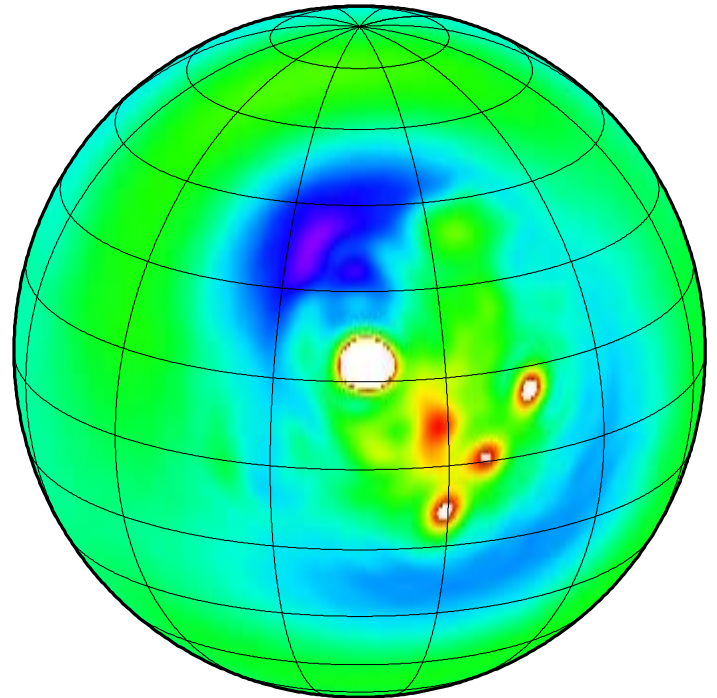
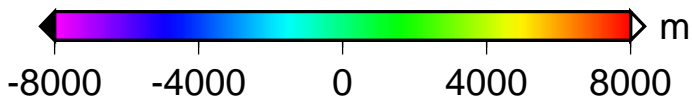


**(c) Gravity: degrees 2 to 60**

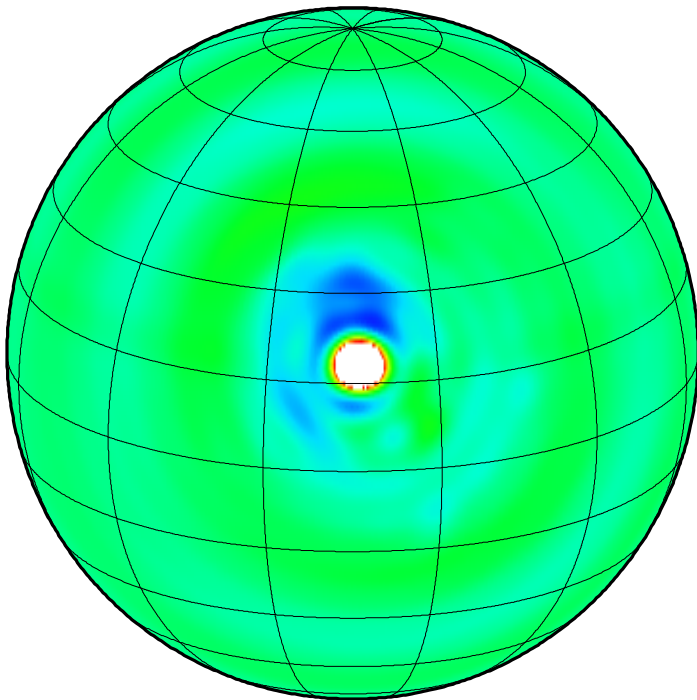
# *Olympus Mons*



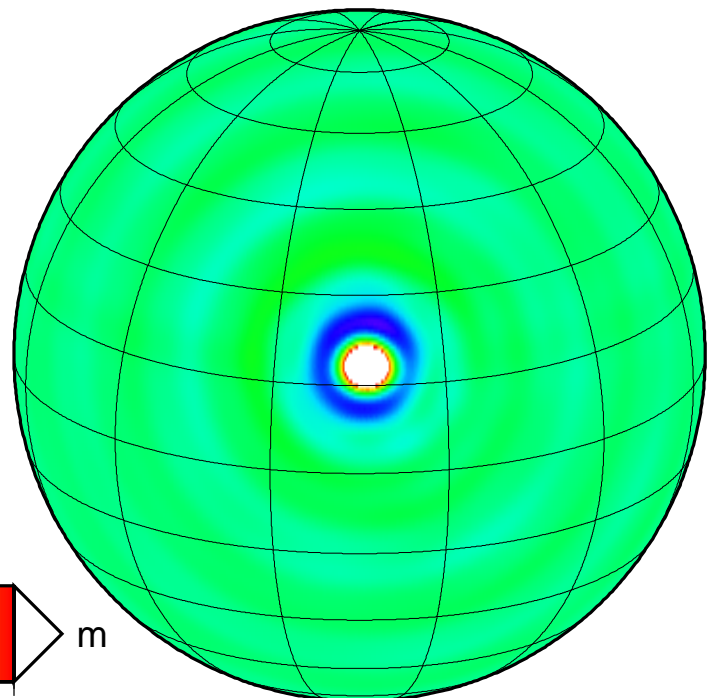
*Shape, degrees 1 to 60*



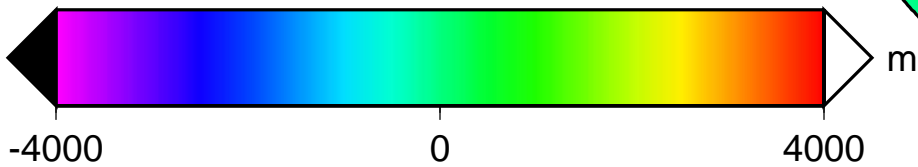
$L_{win} = 5$



$L_{win} = 10$



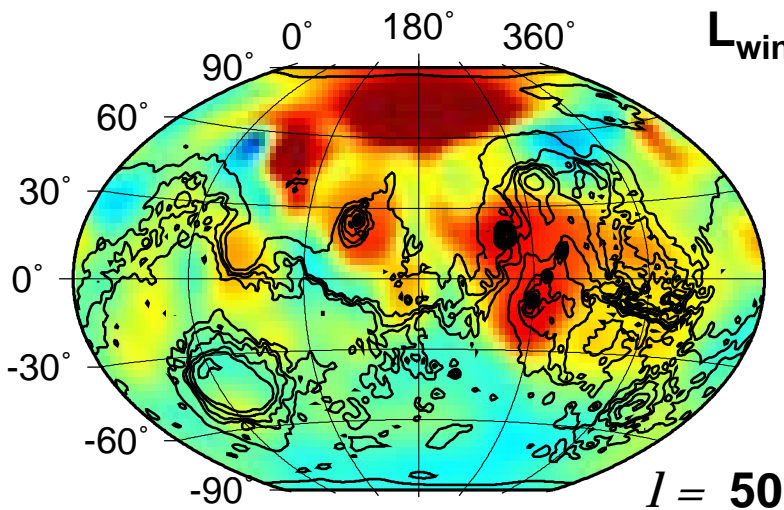
$L_{win} = 15$



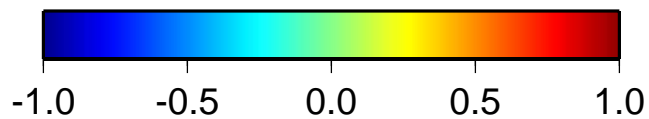
Localized Shape



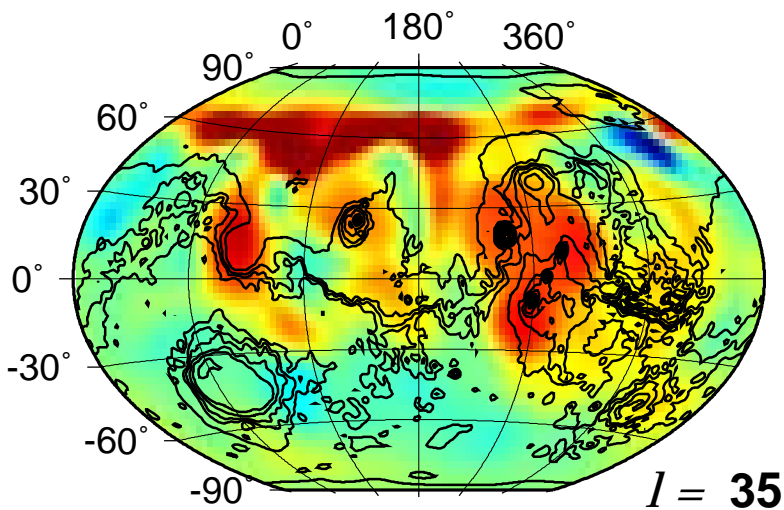
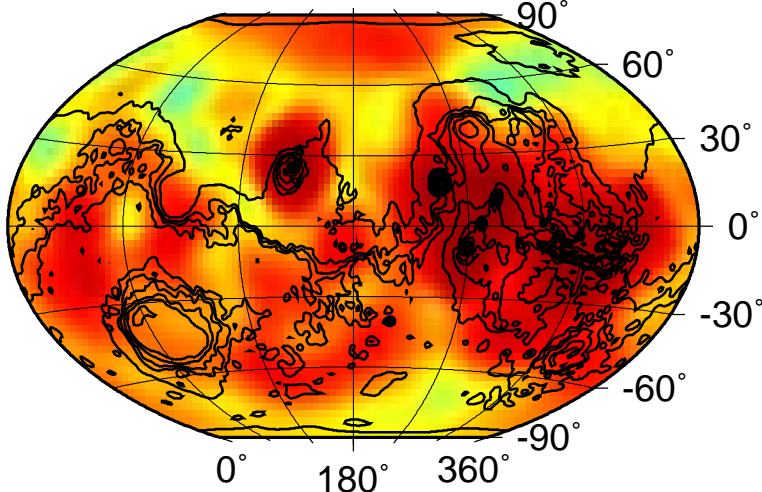
$L_{win} = 10$



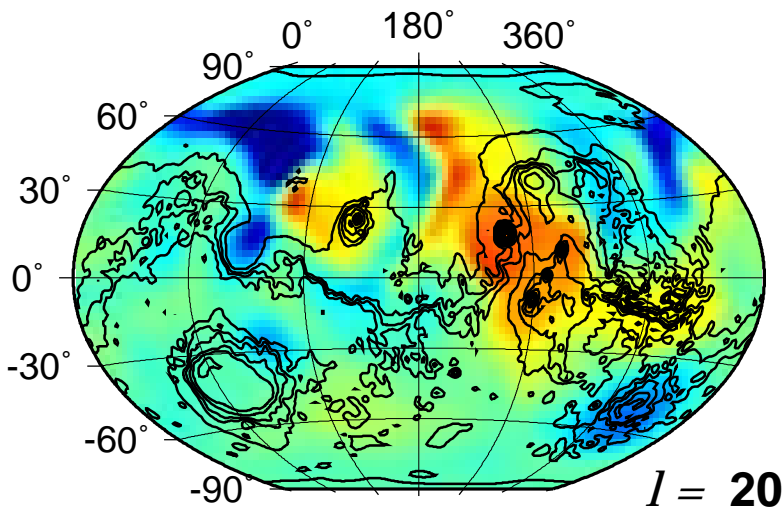
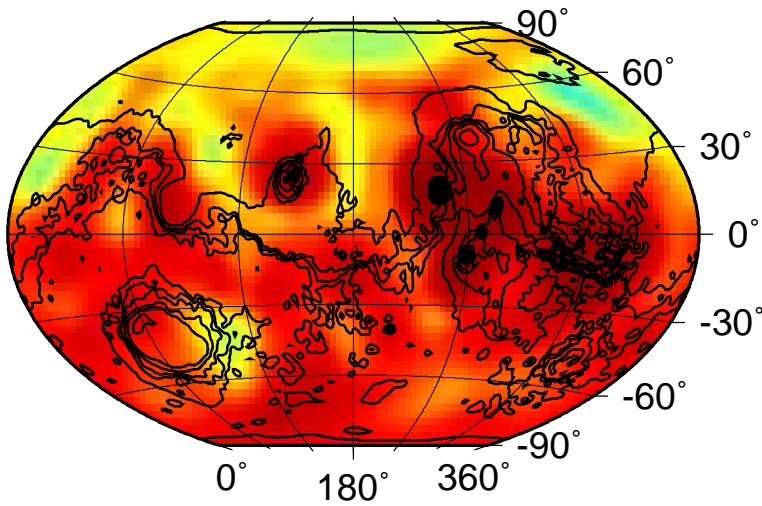
$l = 50$



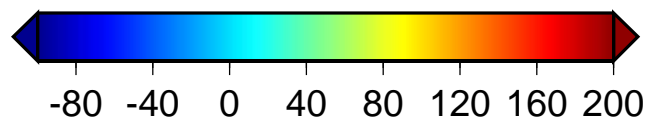
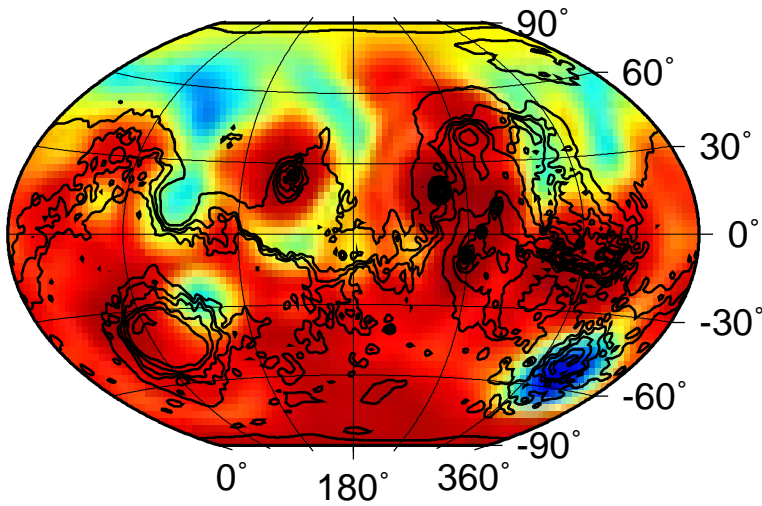
Correlation



$l = 35$



$l = 20$



Admittance (mGal/km)

